Gondwana Research 109 (2022) 493–517

Contents lists available at ScienceDirect

Gondwana Research

journal homepage: www.elsevier.com/locate/gr

Emplacement ages of diamondiferous kimberlites in the Wafangdian District, North China Craton: New evidence from LA-ICP-MS U-Pb geochronology of andradite-rich garnet

Dongsheng Li [a,c], Zhongwei Wu [b,c,d], Xiaoming Sun [a,b,d,*], Song Shuai [a], Yu Fu [b,d], Dengfeng Li [b,d], Hongjun Chen [b], Yang Lu [e], Lubing Hong [c]

[a] School of Earth Sciences and Engineering, Sun Yat-sen University, Zhuhai 519082, China
[b] School of Marine Sciences, Sun Yat-sen University, Zhuhai 519082, China
[c] Gemological Institute, Guilin University of Technology, Guilin 541004, China
[d] Guangdong Provincial Key Laboratory of Marine Resources and Coastal Engineering, Zhuhai 519082, China
[e] Natural History Museum, University of Oslo, Blindern, Oslo 0318, Norway

ARTICLE INFO

Article history:
Received 9 August 2021
Revised 30 April 2022
Accepted 22 May 2022
Available online 26 May 2022
Handling Editor: S. Tappe

Keywords:
Kimberlite
Andradite-rich garnet
LA-ICP-MS U-Pb dating
Wafangdian diamond deposit
North China Craton

ABSTRACT

This contribution presents new U-Pb geochronological data and attempts to elucidate the complex evolution history of various garnet types identified from two kimberlite pipes in the Wafangdian diamond mining district, southern Liaoning Province. These calcic garnets are dominated by andradite with relatively low proportions of schorlomite, grossular and pyrope. Abundant euhedral to subhedral, highly brecciated andradite phenocrysts hosted by LN30 "carbonatite-like" kimberlite samples yield a lower-intercept age of 459.3 ± 3.4 Ma, which is in excellent agreement with the previously reported phlogopite Ar-Ar (463.9 ± 0.9 Ma) and Rb-Sr ages (461.7 ± 4.8 Ma). Based on their trace element and C-O isotopic compositions of associated groundmass carbonate, we infer that these primary magmatic andradites probably originated from kimberlitic magmas. By comparison, three compositionally and texturally distinct groups of Ti-bearing andradites from LN42 hypabyssal kimberlites separately define three well-fitted regression lines with lower intercept ages at 581 ± 12 Ma, 414.9 ± 9.3 Ma and 292.0 ± 5.7 Ma, respectively. Relict andradite xenocrysts implies that ancient lower crust of the North China Craton (NCC) might have been affected by a significant but less-known tectonothermal event to varying degrees at ~ 0.6 Ga. By contrast, fresh grains of magmatic Ti-andradites with chemical zoning produce a relatively young age of ~ 415 Ma, which can still provide minimum age estimates for the most recent pulses of Paleozoic kimberlite magmatism in this study area. Noteworthily, a yet unrecognized local-scale hydrothermal alteration event at ~ 292 Ma has been recorded in the texturally distinct population of secondary hydroandradites, whose age reported here for the first time is geologically meaningful. To sum up, this study further highlights andradite U-Pb dating as a potential robust geochronometer for constraining the late-stage evolution of kimberlite magmas as well as post emplacement hydrothermal alteration.

© 2022 The Author(s). Published by Elsevier B.V. on behalf of International Association for Gondwana Research. This is an open access article under the CC BY-NC-ND license (http://creativecommons.org/licenses/by-nc-nd/4.0/).

1. Introduction

Garnet, a commonly used mineral in geochronology, has the unparalleled ability to record both the conditions and the timing of its growth (Mezger et al., 1989; Baxter and Scherer, 2013; Smit et al., 2013; Seman et al., 2017). It can be dated using multiple approaches, such as the Sm-Nd and Lu-Hf isochrons (Duchêne et al., 1997; Lazarov et al., 2009; Tappe et al., 2011; Koornneef et al., 2017). Compared to the Sm-Nd isotopic system, U-Pb geochronology has a number of distinct advantages. It can be performed using *in-situ* analytical methods, which does not require complementary co-genetic phases or bulk sample measurements to calculate an age. Although ID-TIMS and SIMS U-Pb dating methods may act as powerful tools to obtain garnet ages, these geochronological techniques are often very costly and time-consuming. Until recently, U-Pb dating of garnets (either enriched or depleted in U) with LA-ICP-MS has become available to date the formation ages of skarn deposits (e.g., Deng et al., 2017; Seman

* Corresponding author at: School of Earth Sciences and Engineering, Sun Yat-sen University, Zhuhai 519082, China.
E-mail address: eessxm@mail.sysu.edu.cn (X. Sun).

https://doi.org/10.1016/j.gr.2022.05.016
1342-937X/© 2022 The Author(s). Published by Elsevier B.V. on behalf of International Association for Gondwana Research.
This is an open access article under the CC BY-NC-ND license (http://creativecommons.org/licenses/by-nc-nd/4.0/).

et al., 2017; Fu et al., 2018; Gevedon et al., 2018; Wafforn et al., 2018; Li et al., 2019; Zhang et al., 2019; Yan et al., 2020; Hong et al., 2021; Tang et al., 2021; Reinhardt et al., 2022) and to constrain regional metamorphic history (Millonig et al., 2020; Schannor et al., 2021). Owing to its high spatial resolution and rapid data acquisition, this method has greatly facilitated garnet U-Pb geochronology.

Besides the metamorphic and skarn-related hydrothermal garnets just mentioned, calcic garnets are also ubiquitously present in many silica-undersaturated alkaline plutonic and volcanic rocks (e.g., Huggins et al., 1977; Vuorinen et al., 2005; Scheibner et al., 2007), which may crystallize from residual silicate melts or fluids during the final crystallization stages of ultramafic magma (Vuorinen et al., 2005; Dongre et al., 2016). These magmatic garnets, which represent a complex series of solid solutions (Grew et al., 2013) commonly dominated by andradite ($Ca_3Fe_2Si_3O_{12}$), grossular ($Ca_3Al_2Si_3O_{12}$), schorlomite ($Ca_3Ti_2SiFe_2O_{12}$), morimotoite ($Ca_3TiFeSi_3O_{12}$) and kimzeyite ($Ca_3Zr_2SiAl_2O_{12}$), seem to have been largely neglected as a potential U-Pb geochronometer by isotope geochemists until recent years. Previously, in his pioneering work on Archean ultramafic lamprophyres, Barrie (1990) demonstrated that Ti-bearing andradite retains its initial U-Pb isotopic systematics in old igneous rocks subjected to deformation. So far, it has been confirmed that calcic garnets have some distinct advantages over aluminous garnets (Mezger et al., 1989, 1991; Seman et al., 2017; Salnikova et al., 2019), and thus represent ideal multi-system geochronological tools as well as petrogenetic indicators because they (1) can host elevated levels of U, Th, Hf and rare earth elements (REEs), (2) contain low levels of common Pb, and (3) occur in a wide variety of rocks (Deng et al., 2017; Salnikova et al., 2019; Millonig et al., 2020). For example, primary calcic garnets enriched in andradite-schorlomite-morimotoite-kimzeyite components have been found in ultramafic lamprophyres (Barrie, 1990; Tappe et al., 2004, 2005, 2006), intrusive carbonatite complexes as well as pyroxenite-ijolite-nepheline syenite-series (Vuorinen et al., 2005; Tappe et al., 2009; Rukhlov and Bell, 2010; Salnikova et al., 2018a, 2018b, 2019; Yang et al., 2018; Stifeeva et al., 2020; Reguir et al., 2021). Interestingly, they were once considered comparatively rare but nowadays appear to be rather common in the groundmass of kimberlites and related orangeites or lamproites with many more cases reported in the literature (e.g., Cheng et al., 2014; Dongre et al., 2016; Shaikh et al., 2017; Dongre and Tappe, 2019; Choudhary et al., 2020; Tappe et al., 2022).

Kimberlites, the dominant source of diamonds worldwide, are a variety of rare, small-volume, potassic and volatile-rich ultramafic rocks that originate from either the deep lithosphere or sub-lithospheric mantle (Mitchell, 1986, 1995; Woolley et al., 1996; Giuliani and Pearson, 2019). It is widely accepted that the most likely settings for the emplacement of diamond-bearing kimberlite pipes are Archaean cratons. In addition to being the carriers of diamonds and mantle xenoliths, kimberlite magmas can also provide insights into deep Earth processes, including the links between cratonic metasomatism and low-degree partial melting (Donnelly et al., 2012; Pearson et al., 2019). However, more comprehensive or detailed studies of kimberlites are often hampered by their hybrid nature and post-intrusion alteration (Mitchell et al., 2019). High volatile contents make kimberlites particularly susceptible to weathering. Moreover, the presence of xenoliths and xenocrysts entrained from the mantle or crust may result in disturbed, mixed and inherited ages, which can complicate the determination of initial isotopic compositions (Donnelly et al., 2012). According to an updated kimberlite geochronology database compiled by Tappe et al. (2018a), only about 20% of the known kimberlite occurrences worldwide have high-quality published age information, as revealed by the temporal distribution of global kimberlite magmatism with available age constraints (see Fig. 1). Thus, the problems of dating kimberlites and understanding their sources continue to be an important research focus at present.

Up to now, the technique of U-Pb geochronology by LA-ICP-MS has been applied on a number of accessory minerals isolated from kimberlites and mantle xenoliths (e.g., apatite, baddeleyite, perovskite, rutile, titanite, and mantle zircon), with varying degrees of success (Heaman et al., 2019). As a ubiquitous groundmass phase in many kimberlites, garnet is generally considered to be highly resistant to post-crystallization interactions with fluids and weathering (Mezger et al., 1989). This makes garnets particularly useful for understanding multi-stage evolution of kimberlitic melts. Therefore, age information deduced from calcic garnets makes it possible to decipher the number of crystal growth and metamorphic/metasomatic episodes within the host kimberlites. However, the application of LA-ICP-MS garnet U-Pb geochronology to constrain the emplacement ages of kimberlites has been relatively limited, especially when compared to the well-developed perovskite (Batumike et al., 2008; Yang et al., 2009; Griffin et al., 2014; Tappe et al., 2018b) and other accessory mineral U-Th-Pb geochronometer (e.g., rutile: Schmitz and Bowring, 2003; Tappe et al., 2014; Malkovets et al., 2016; Schmitt et al., 2019; titanite: Lehmann et al., 2007; Agashev et al., 2016; zircon/baddeleyite: Zheng et al., 2004; Li et al., 2011).

The timing of diamondiferous kimberlites and related magmatism in the North China Craton (NCC) has been extensively investigated by determining perovskite U-Pb and phlogopite Rb-Sr isochron ages for a suite of kimberlite samples collected from central Shandong and southern Liaoning regions (Dobbs et al., 1991; Lu et al., 1995, 1998; Zhang and Yang, 2007; Yang et al., 2009; Li et al., 2011). A summary of these published results indicate that the duration of Paleozoic kimberlitic magmatism mainly occurred during the middle to late Ordovician period within a time span of more than 40 Ma (e.g., Dong, 1991; Lu et al., 1995, 1998). However, there are still some debates on the emplacement ages of Mengyin and Wafangdian kimberlites (erupted on opposite sides of the *trans*-lithospheric Tan-Lu fault), which have not been well constrained by high-precision dating methods until recently. Up to now, available geochronological data have yielded a wide range from ~ 480 to 460 Ma even based on *in-situ* LA-ICP-MS and SIMS analyses. For example, the Mengyin kimberlites are generally considered to have intruded the wall rocks at 465 Ma according to phlogopite Ar-Ar dating (Zhang and Yang, 2007), whereas some authors thought that the emplacement age of Wafangdian kimberlites should be 480 Ma based on baddeleyite Pb-Pb dating (Li et al., 2011).

Our study is the first attempt to apply the U-Pb garnet geochronometer on diamondiferous kimberlites in southern Liaoning Province, China. We present new geochronogical data of U-bearing andradite from the No. 30 and No. 42 pipes to further constrain the emplacement history of kimberlites in the Wafangdian (diamond) mining district. We have also collated other available published age data and relevant information on these kimberlitic intrusions to provide an evaluation of the reliability of andradite-rich garnet U-Pb ages. In cases of the Wafangdian kimberlites where perovskite and other relatively U-rich accessory minerals (suitable for dating) are unavailable, we demonstrated that even for variably altered kimberlites, high-precision garnet U-Pb ages can be obtained using a laser ablation system coupled to an ICP-MS instrument. Hence, this work is expected to shed some light on broadening the application of U-Pb garnet geochronometer to earth sciences.

2. Geological background

The North China Craton is one of the oldest tectonic units in China with crustal components up to 3.8 Ga and provides the most

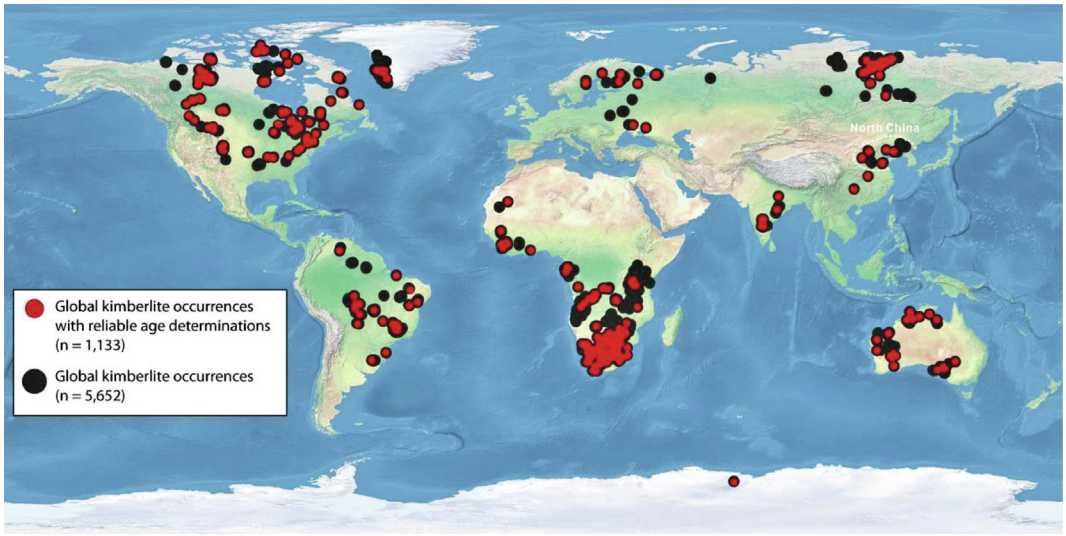

Fig. 1. World map showing the global distribution of kimberlites (grey dots; n = 5652). About one-fifth of their occurrences have available and reliable age information in the public domain (red dots, n = 1133), which are based on a recently updated global database cited from Tappe et al. (2018a). Note that this diagram also highlights the locations (as indicated by white dash lines) of regional kimberlite fields in relation to primary diamond deposits on the eastern North China Craton (NCC). (For interpretation of the references to color in this figure legend, the reader is referred to the web version of this article.)

favorable environment for diamond occurrence, which is bounded by the Late Paleozoic Central Asian Orogenic Belt to the north, the Early Paleozoic Qilian Orogen to the west and the Qinling-Dabie-Sulu ultrahigh-pressure metamorphic belt to the south (Liu et al., 1992; Song et al., 1996; Zhao and Zhai, 2013; Zhu et al., 2017). The nature and evolution of the NCC were described in detail by previous investigators (Gao et al., 2002; Wu et al., 2003; Zhao et al., 2002, 2005; Zheng et al., 2004). There are two diamondiferous kimberlite fields, Mengyin and Wafangdian (originally called Fuxian County), located at the southeastern and northeastern margin of the NCC, respectively (Fig. 2A). More than 50% of the discovered diamond reserves are locally concentrated in southern Liaoning Province (Liu et al., 2020).

The Wafangdian kimberlites predominantly intrude into Upper Proterozoic sedimentary rocks in eastern Liaoning Peninsula of the Ji-Lu-Liao continental nucleus, about 80-km east of the Tan-Lu fault zone. Currently, the studied No. 30 and No. 42 kimberlite pipes are being commercially mined for diamonds, which belong to the Wafangdian diamondiferous field (including nearly 110 kimberlitic bodies). As shown in Fig. 2B, there are three parallel diamondiferous kimberlite belts oriented northeast-southwest in this area, which consist of many kimberlite pipes occurring as carrot-shaped vertical intrusions and tabular dykes known as fissure kimberlites (Zhu et al., 2017, 2019a, 2019b; Fu, 2020; Ni and Zhu, 2020). The strata intruded by kimberlites in our study area comprise an Archean-Paleoproterozoic basement named the Liaohe Group (which includes amphibolite and gneiss), and Neoproterozoic cover rocks named the Qingbaikou Formation (which consists of limestone, shale and sandstone). A few Ordovician limestone rocks also occur as country rocks (Fig. 2B).

The North China Craton was stable until early Paleozoic kimberlitic magmatism took place. The Mengyin and Wafangdian kimberlites are generally considered to have intruded the local wall rocks simultaneously at about 465 Ma, according to phlogopite Rb-Sb and Ar-Ar dating (Li et al., 2005; Zhang and Yang, 2007). However, Li et al. (2011) suggested that the emplacement of these kimberlites should be occurred at an even earlier age (~480 Ma) based on baddeleyite Pb-Pb dating. Although the Wafangdian kimberlites contain abundant mantle-derived xenoliths, almost all olivines found in the No. 30 and No. 42 pipes are intensively altered. Only a few selected minerals, such as garnet phenocrysts, survived kimberlitic magmatism. Hence, the unusual presence of calcic garnets (either as cratonic xenocrysts or as a late-crystallizing phase replacing the groundmass atoll spinels/magnetite in some cases) within partially altered rock samples collected from this kimberlite field may provide an opportunity to study the evolutionary history (e.g., deep crustal metamorphism/mantle metasomatism) of ancient continental lithosphere beneath the eastern North China Craton.

In this study, most of the selected hand specimens are variably altered, with a subset of samples exhibiting partial to complete replacement of the primary mineral assemblage by serpentine and/or carbonates. In contrast to the Wafangdian No. 30 kimberlite pipe (strongly altered by low-temperature serpentinization and carbonatization), the No. 42 pipe mainly consists of macrocrystal kimberlites and brecciated facies with a few fine-grained varieties, which contain relatively high percentages of phlogopite megacrysts and phenocrysts. In other words, these macrocrystal phlogopite kimberlites are regarded as transitional between those of Group I and Group II in terms of phlogopite contents as well as Sr-Nd isotopic compositions (Zhang and Yang, 2007). Detailed descriptions of local kimberlite pipes (rock types and petrographical-mineralogical characteristics) are available in Dong (1991), Tompkins et al. (1998), Zhang et al. (2010), Zhao et al. (2015), Zhu et al. (2017, 2019a, 2019b, 2022), Liu et al. (2020), Ni and Zhu (2020), and Wang et al. (2020).

3. Samples and analytical methods

3.1. Sample preparation and EPMA measurements

Garnet crystals collected from the No. 30 and No. 42 kimberlite pipes were separated using magnetic and heavy-liquid separation methods, followed by hand-picking under a binocular microscope. More than 100 grains were encased in epoxy resin mounts, carefully polished, and then photographed under both transmitted and reflected light of optical microscopy. Thin sections were also prepared for the kimberlite samples, which were examined with optical microscopy and back-scattered electron (BSE) imaging.

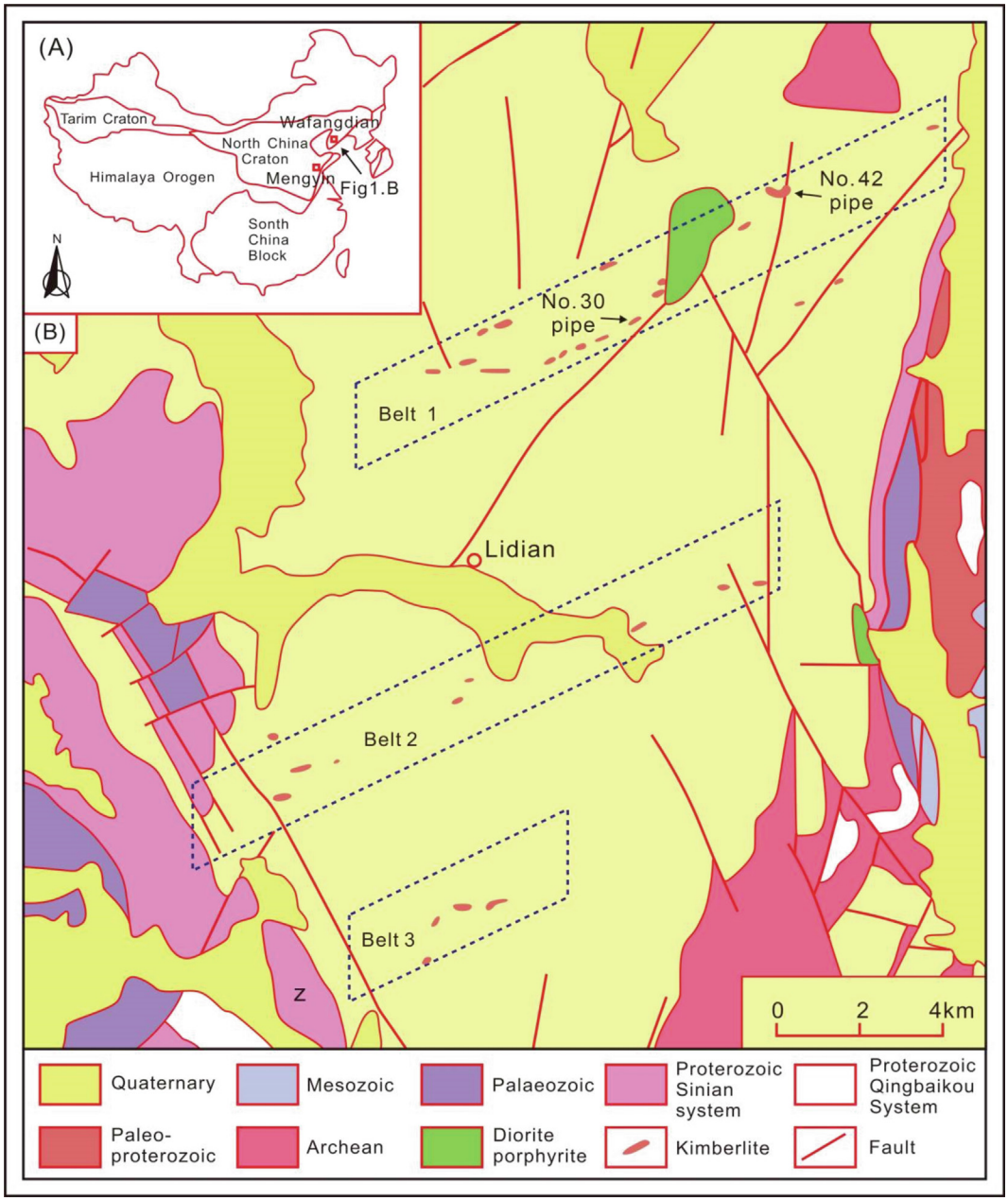

Fig. 2. (A) Simplified tectonic subdivisions of China and the localities of Wafangdian and Mengyin (red open square symbol) diamondiferous kimberlite fields on the eastern North China Craton; (B) Geological map modified after Zhu et al. (2019b) showing the locations of No. 30 and No. 42 kimberlite pipes in the Wafangdian mining district. (For interpretation of the references to color in this figure legend, the reader is referred to the web version of this article.)

BSE imaging was carried out using a Zeiss ΣIGMA field-emission scanning electron microscope (FE-SEM) at the School of Earth Sciences and Engineering, Sun Yat-sen University (China). Prior to the LA-ICP-MS analysis, major element abundances of these garnet crystals were determined using a Shimadzu 1720H electron probe micro-analyzer (EPMA) at the Key Laboratory of Geoscience Big Data and Deep Resource of Zhejiang Province, School of Earth Science, Zhejiang University. Operating conditions were performed at an accelerating voltage of 15 kV with a beam current of 20nA. A beam diameter of 5 μm was used for quantitative elemental determination in carbon-coated specimens. The counting time was 30 s for on-peak and 10 s for off-peak background measurements. Natural and synthetic oxides/silicate minerals were used as reference materials for calibration. Matrix correction was done using the ZAF routines.

3.2. SEM-based TIMA and μ-XRF mapping

Rapid semi-quantitative mapping of mineralogical composition was obtained on selected areas in carbon-coated thin sections using a MIRA3 scanning electron microscope equipped with a TESCAN Intergrated Mineral Analyzer (TIMA) at Guangzhou Tuoyan Analytical Technology Co., Ltd. (China). We use an acceleration voltage of 25 kV and a probe current of 20nA. Working distance was set to 15 mm. Pixel resolution and dot spacing was set to 3 μm and 9 μm, respectively. The current and BSE signal intensity were calibrated on a platinum Faraday cup using automated procedures. The performance of energy-dispersive X-ray spectrometer (EDS) was checked using manganese standard. Typical garnet-bearing kimberlite samples LN30 and LN42 were scanned using SEM-based mineral liberation analysis (MLA) module.

Furthermore, to gain detailed knowledge of chemical composition at the hand-specimen scale (containing the mineral assemblage of interest), elemental distribution maps were collected from two representative polished thin sections by *in-situ* quantitative analysis using a Bruker M4 Tornado micro-beam X-ray fluorescence (μ-XRF) spectrometer equipped with polycapillary X-ray optics (operated at 50 kV and 300 μA).

3.3. Carbon and oxygen isotope analyses

In addition to petrographic and mineralogical analyses, stable isotopic signatures of twelve garnet-bearing kimberlite subsamples were investigated at the Key Laboratory of Marine Resources and Coastal Engineering, Sun Yat-sen University. Whole-rock powders and micro-drilled samples (~200 μg) obtained from thick polished slabs of carbonate-rich kimberlites were converted to CO_2 by reacting with 100% phosphoric acid at room temperature (25 °C) for 24 h. Subsequently, their carbon and oxygen isotopic compositions were determined by a Thermo Scientific MAT 253 Plus isotope ratio mass spectrometer (IRMS) coupled with a GasBench II system, then calibrated with international reference materials NBS-18 (with a precision better than ± 0.2‰) and are reported in conventional δ notation relative to the reference standard V-PDB and V-SMOW, respectively. The corresponding major and trace element abundances in selected bulk specimens were measured by ALS Chemex (Guangzhou) Co., Ltd. using test method Code Nos. "P61-XRF15c" and "REE-TCE02".

3.4. Garnet LA-ICP-MS U-Pb dating and trace element analysis

In-situ U-Pb dating and trace element analysis of the Wafangdian garnet samples were performed by LA-ICP-MS using an Analytik Jena Aurora M90 quadrupole ICP-MS coupled to a NWR193 (ESI) 193-nm ArF excimer laser at Beijing Yanduzhongshi Geological Analysis Laboratories Ltd. (China). Laser-induced downhole fractionation, instrumental drift and mass bias correction factors for Pb/U ratios on andradite-grossular garnets were determined using Mali grandite and Willsboro andradite as primary and secondary U-Pb standards, respectively. Such garnets are both characterized by low common lead and relatively low contents of U and Th, which showed consistent elemental fractionation behavior, thus allowing for an accurate downhole-fractionation correction (Seman et al., 2017). For data quality control, an in-house standard (ZSLS Ti-rich garnet) was also analyzed along with these two certified reference materials to independently monitor the external precision and accuracy of LA-ICP-MS measurements (Supplementary Table S5). The reference garnet crystals were analyzed at the beginning of each session and every 10 unknown andradite-grossular garnets, adopting the same laser-beam spot size (45 μm for hand-picked individual grains and 35 μm for polished thin sections) and operation conditions as those used on the test specimens (laser pulses at 9 Hz with an energy density of approximately 3 J/cm^2).

Each analysis began with a 20-second laser-off background (gas blank) measurement followed by a further 40-second of data acquisition time when the laser was switched on. High-purity helium was used as the carrier gas at a flow rate of 0.6 L/minute, which transported laser-ablated materials out of the chamber. Then the sample aerosol particles were introduced into the plasma torch by a continuous flow of helium mixed with argon gas. Isotopes measured included ^{202}Hg, ^{204}Pb, ^{206}Pb, ^{207}Pb, ^{208}Pb, ^{232}Th and ^{238}U. Each element was measured sequentially every 0.18 s with a longer counting time on the Pb isotopes compared to the other elements. Data reduction was based on the method outlined in detail in Meffre et al. (2008), with an additional modification to help correct for the small amount of common Pb present in the primary standard using the ^{207}Pb correction approach as recommended by Chew et al. (2011, 2014), which either adopted an initial Pb isotopic composition by analyzing a low-U cogenetic mineral phase with negligible ingrowth of radiogenic Pb or typically used appropriate terrestrial Pb evolution models in the literature (e.g., Stacey and Kramers, 1975).

For comparison, *in-situ* elemental analyses were also conducted at the Key Laboratory of Marine Resources and Coastal Engineering, SYSU using an ArF excimer laser ablation system (GeoLasPro) coupled with an Agilent 7900 ICP-MS. A 44-μm spot size was used with an energy density of 5 J/cm^2 and a repetition rate of 5 Hz. The trace element concentrations of LN30 and LN42 garnet samples were calibrated against the external standard NIST SRM-610 glass and quantified using ^{29}Si (determined by EPMA or assumed in stoichiometric proportions) as an internal standard element. The calculated LA-ICP-MS results were then compared with EPMA data to check the precision and accuracy. Data reduction was performed using Iolite software (Paton et al., 2011). IsoplotR software was used to construct the Tera-Wasserburg concordia diagram, see Vermeesch (2018) and references therein.

4. Results

4.1. Garnet petrography

The garnet specimens recovered from the No. 30 and No. 42 kimberlite pipes are dominated by medium- to coarse-grained titaniferous andradite crystals, either monocrystalline or polycrystalline, and range in size from < 0.1 mm to ~ 1 mm in maximum dimension. These garnet samples appear to be reddish brown in color under plane-polarized light, typically displaying deformation features. They are often found to coexist with a substantial proportion of carbonates mainly consisting of anhedral calcite, and olivine pseudomorphs replaced by serpentine, as well as minor amounts of phlogopite, apatite, chlorite, magnetite and/or Fe-Cr spinel clusters (Fig. 3A and B).

In LN30 carbonatized kimberlite samples, andradites are essentially isotropic and occur as euhedral to subhedral phenocrysts (200–500 μm), or occasionally as larger megacryst fragments up to 1 mm in size. They are commonly enclosed in a carbonate-rich matrix with micro-cracks and veinlet networks infilled by late-stage calcite, and closely associated with remnants of partially serpentinized olivine, altered phlogopite or accompanied by a variety of irregularly shaped, earlier-formed Mg-Al-rich silicate phases (similar to pyrope in chemical composition) along fractures (Fig. 4A and B). Some individual crystals contain euhedral-shaped olivine, prograde polygonal serpentine and fine-grained phlogopite inclusions (Fig. 4C – 4F). Under SEM, no discernible patchy zoning, dissolution–recrystallization or overgrowth textures were observed within these heavily brecciated andradites in the BSE mode (Fig. 4).

By comparison, at least three generations of andradite-rich garnets (see Figs. 5 and 6) have been identified in LN42 kimberlite serpentinized samples according to their occurrence modes, textures, mineral paragenesis, and compositional differences among these garnet types (as an important distinguishing feature, this issue is further discussed in the next section). The oldest generation of garnet (referred to as LN42 Grt-I) mostly occurs as discrete anhedral grains and relict fragments of andradite xenocrysts (200–500 μm), or occasionally as distinct first-nucleated cores (with ragged edges/sharp or diffuse replacement fronts at core-mantle boundary) but only rarely preserved in some coarse-grained euhedral grandite garnets with chemical zoning (Fig. 5A–D). The second generation (LN42 Grt-II) is represented by euhedral to subhedral, slightly zoned phenocrysts of Ti-rich andradite (Fig. 5E and F).

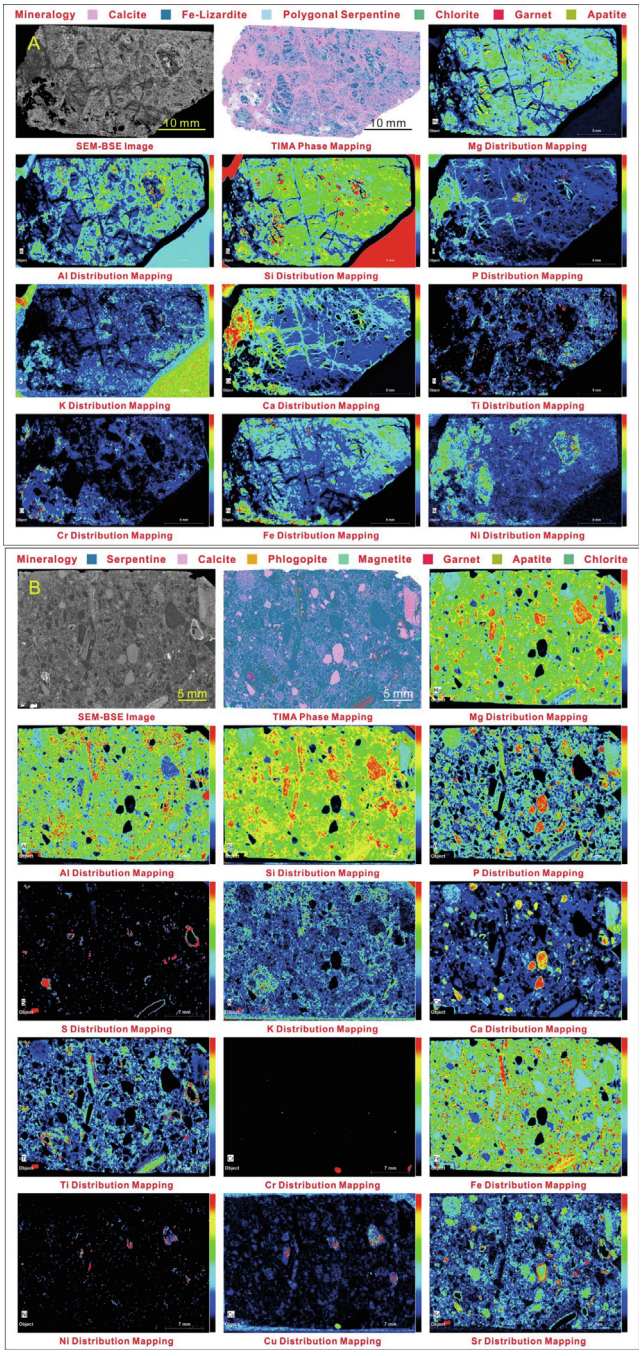

Fig. 3. (A) & (B) SEM-BSE images, TIMA mineralogical analyses and corresponding micro-XRF elemental distribution maps of representative kimberlite thin-section specimens from the Wafangdian No. 30 and No. 42 pipes. Locally, some carbonate segregations occur as masses of coalescent spherulites in the silicate-dominated matrix and, more rarely, silicate-rich globules (or irregular patches) associated with late-stage calcite veinlets.

Most of them have been partially or completely replaced by later-formed, irregular-shaped andradite (cogenetic with LN42 Grt-III, as described below), usually coexisting with magnetite, chlorite and/or serpentine group minerals within a calcite matrix (Fig. 5G). To a lesser extent, some Grt-II grains contain resorbed inherited Grt-I cores overgrown by infiltration-driven metasomatic reaction domains (Fig. 5A).

The most common type of calcic garnet encountered in the No. 42 pipe is characterized by a group of corroded andradite microcrysts originated from the disaggregation of xenocrystic Grt-I precursors (LN42 Grt-III). They are apparently unzoned, mostly free of inclusions and appear to be more rounded in shape, which commonly show morphological similarities to Grt-I xenocrysts and display porous spongy textures (Fig. 5H and I). Their grain boundaries and surrounding matrix are often accompanied by clastic Mg-Al silicate minerals (alteration products), occasionally coexisting with groundmass Ti-magnetite/ilmenite, apatite, fine-grained intergrowth of rutile and titanite, as well as sporadic pyrite or other sulfides (Fig. 5H–L). Resorbed spinel crystals with well-developed atoll textures have also been observed in the host kimberlite, which consist of euhedral titanian-chrome-magnetite core isolated from the rim of magnetite-andradite by spongy lagoon phases containing serpentine and/or calcite (as shown in Fig. 5K), probably caused by partial resorption/dissolution and replacement reactions. In addition, it should be noted that some millimeter- to submillimeter-sized, silicate-rich globules contain corroded relicts of Grt-I aggregates (similar in appearance to carbonate-serpentine segregations or xenoliths with unique nodule-like structures), which are rimmed by thin mantle of groundmass Grt-III clasts and pre-existing rutile-titanite-magnetite assemblages as well as secondary mineral phases including retrograde lizardite and/or minor chlorite (Fig. 5L).

4.2. Major and trace element chemistry

Major element compositions of the Wafangdian garnets are summarized in Supplementary Table S1 (N = 105). Overall, calcic garnets from the No. 30 pipe have fairly constant SiO_2 (34.64 – 35.87 wt%), CaO (32.33 – 33.48 wt%) and FeO_{Total} (23.82 – 26.47 wt%), with average values of 35.37 wt% SiO_2, 32.93 wt% CaO and 24.88 wt% FeO (N = 49), respectively. They exhibit relatively low Al_2O_3 (0.40 – 1.86 wt%) and TiO_2 (0.38 – 2.94 wt%), with average concentrations of 1.17 wt% Al_2O_3 and 1.05 wt% TiO_2, respectively. The chemical structural formulae for these kimberlite-hosted garnets were calculated from EPMA data by normalizing to 8 cations on the basis of 12 oxygen atoms per formula unit. The low analytical totals are a consequence of all Fe being reported as FeO. As shown in Fig. 6, the LN30 garnet samples mostly belong to the andradite-grossular-schorlomite solid solution series ($Adr_{85.92\text{-}92.98}Slm_{1.11\text{-}9.23}Grs_{0.0\text{-}9.16}Prp_{1.52\text{-}4.64}$) with minor amounts of spessartine (average = ~0.1%) and uvarovite (average = ~0.1%) components. As revealed by EPMA spot analyses across a number of individual grains (see Supplementary Fig. S1), their main chemical constituents appear to be generally homogeneous. Despite that, the variabilities of Mg and Ti from the interior parts towards the grain margins (Fig. 7A) seem to be more pronounced than the phenomenon of Si-Ca-Fe zoning, even though no discrete internal zones could be easily distinguished by BSE imaging because of the subtle difference in average atomic number.

Similarly, calcic garnets from the No. 42 pipe contain substantial but not uniform SiO_2 (31.56 – 37.17 wt%), CaO (33.20 – 35.50 wt%) and FeO_{Total} (20.25 – 25.94 wt%) as well as relatively low Al_2O_3 (0.99 – 3.92 wt%) and TiO_2 (0.11 – 3.40 wt%), with average values of 34.53 wt% SiO_2, 33.95 wt% CaO, 23.26 wt% FeO, 2.38 wt% Al_2O_3 and 1.13 wt% TiO_2 (N = 56), respectively. Although Cr_2O_3 and MnO are both detectable, their contents do not exceed 0.2 wt%. By comparison, the LN42 garnet samples display a wider compositional range dominated by andradite end-member component with variable but still relatively low proportions of grossular, schorlomite and pyrope ($Adr_{76.50\text{-}91.01}Grs_{3.25\text{-}20.60}Slm_{0.30\text{-}9.80}Prp_{1.21\text{-}4.80}$). It is noteworthy that the three generations of LN42 garnets mentioned above are more heterogeneous in major element chemistry than those LN30 andradites, as clearly shown in Figs. 6 and 8A (LN42 Grt-I: $Adr_{87.90\text{-}91.01}Grs_{3.25\text{-}5.68}Slm_{1.88\text{-}5.17}Prp_{1.76\text{-}2.79}$; LN42 Grt-II: $Adr_{76.74\text{-}83.68}Grs_{8.11\text{-}15.31}Slm_{3.27\text{-}9.80}Prp_{2.10\text{-}4.80}$; LN42 Grt-III:

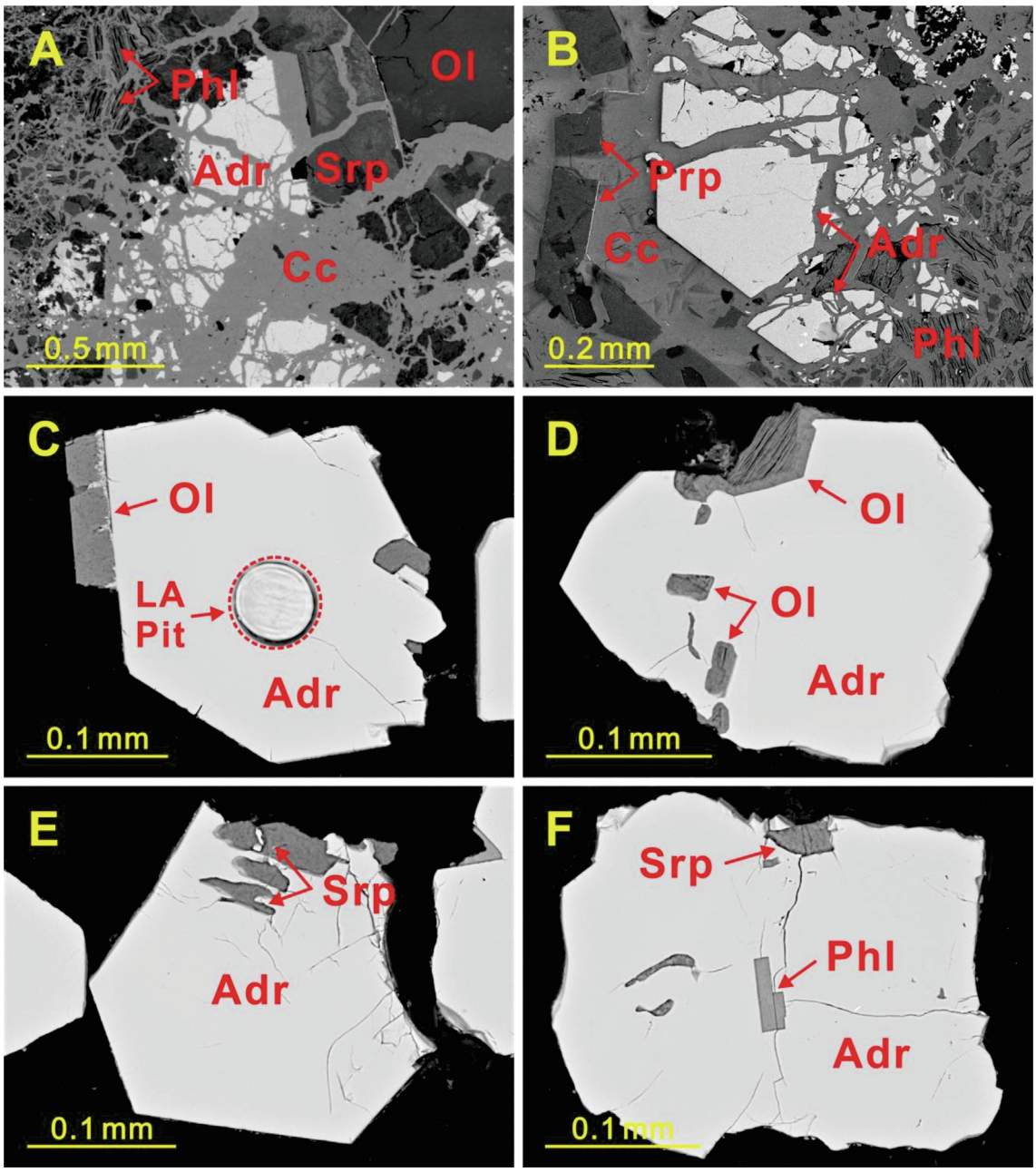

Fig. 4. (A) & (B) Occurrences and distribution of fragmented garnet grains in polished thin-section specimens from the No. 30 kimberlite pipe. Note that most of these andradite-rich garnet crystals are commonly cracked and filled with or enclosed by carbonate veins cross-cutting the groundmass. (C) - (F) Euhedral- to subhedral-shaped, individual andradite phenocrysts (200–500 μm) closely associated with relict olivine and typically polygonal serpentine (intermixed with Fe-lizardite/chrysotile) or containing fine-grained phlogopite inclusions. Back-scattered electron (BSE) images show the absence of recrystallization or overgrowth textures and no discernible patchy zoning within these heavily brecciated, compositionally homogeneous andradites, probably suggestive of a single episode growth. Circular features observed in some garnet crystals are pits produced by laser ablation (Adr: andradite; Cc: calcite; Ol: olivine; Phl: phlogopite; Prp: pyrope; Srp: serpentine).

$Adr_{76.50\text{-}88.47}Grs_{8.72\text{-}20.60}Slm_{0.30\text{-}2.99}Prp_{1.21\text{-}4.59}$). In addition, the re-calculated totals of some irregular-shaped/rounded, partially to highly altered LN42 Grt-III grains are comparatively lower (~96.0 wt%) than those of fresh LN30 Grt phenocrysts with excellent quality EPMA data, probably indicating the presence of volatile/hydrous components (e.g., structural OH^-) in these hydrogarnet grains (presumably as so-called "hydroandradite").

The trace element results of LA-ICP-MS measurements in garnets are presented in Supplementary Table S2. For LN30 samples, a total of 35 analytical spots were located on fresh garnet grains displaying more euhedral outlines. Overall, most andradite grains contain U at the ppm level (0.30–12.04 μg/g) with an average value of 3.77 μg/g, while Th concentrations range from 0.59 to 25.60 μg/g (on average 4.87 μg/g) with an average Th/U ratio of 2.17. Besides that, their total REE (ΣREE) concentrations range from 170.94 to 660.69 μg/g, with an average content of 345.53 μg/g. Based on the relative positions of laser ablation pits and/or EPMA spots, a set of data points obtained from different garnet domains (roughly defined as "inner cores", "mantle regions/intermediate zones" and "outer rims") can be further separated into three subgroups. It appears that representative andradite phenocrysts are slightly zoned with respect to the distribution of REEs and other trace elements. For example, the compositional evolution trends (shown by the bold arrows in Fig. 7A–F) exhibit continuous decreases in

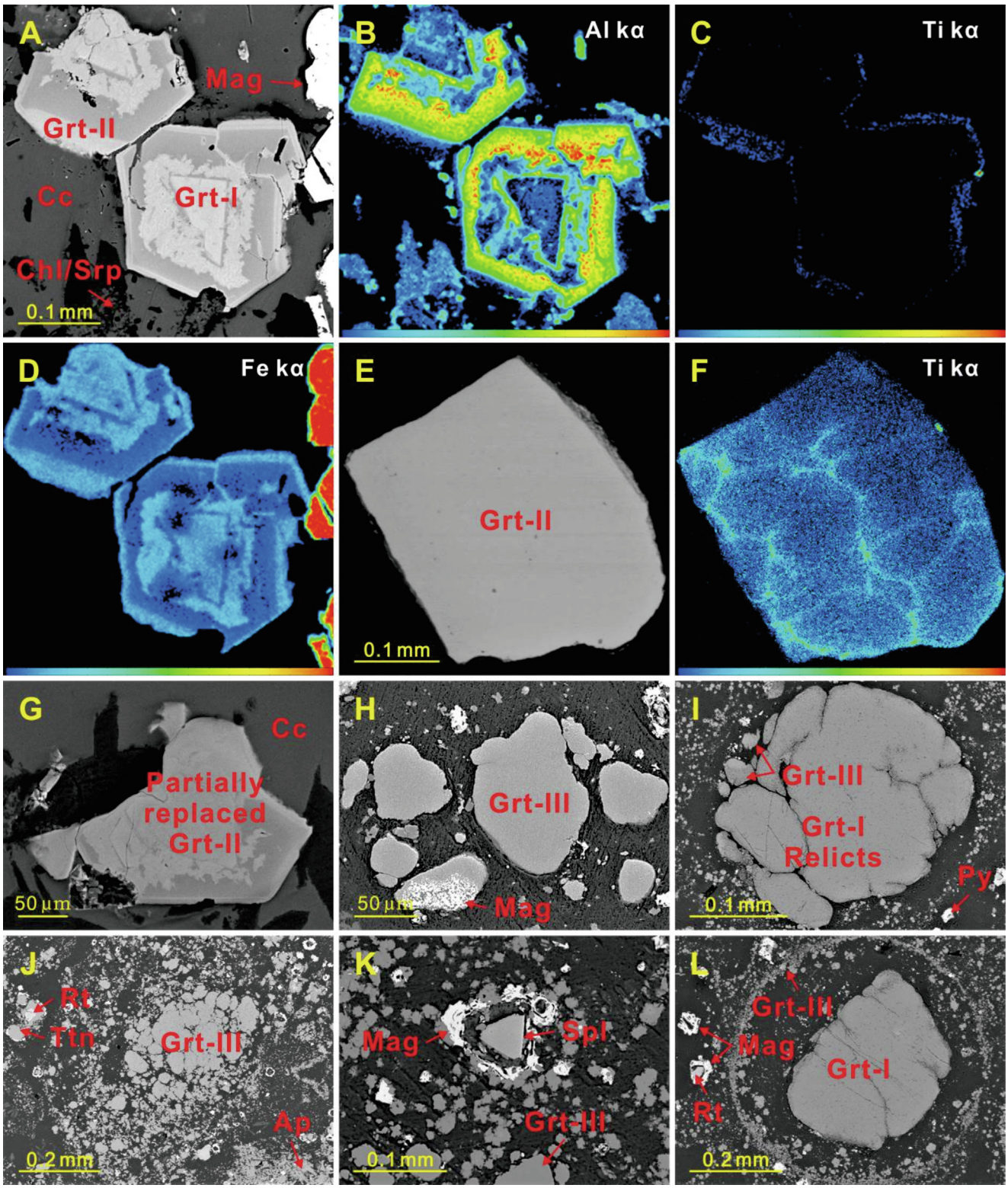
A
Mag
Grt-II
Cc
Grt-I
Chl/Srp
0.1 mm
B
Al kα
C
Ti kα
D
Fe kα
E
Grt-II
0.1 mm
F
Ti kα
G
Cc
Partially replaced Grt-II
50 μm
H
Grt-III
50 μm
Mag
I
Grt-III
Grt-I Relicts
Py
0.1 mm
J
Rt
Ttn
Grt-III
Ap
0.2 mm
K
Mag
Spl
Grt-III
0.1 mm
L
Grt-III
Mag
Grt-I
Rt
0.2 mm

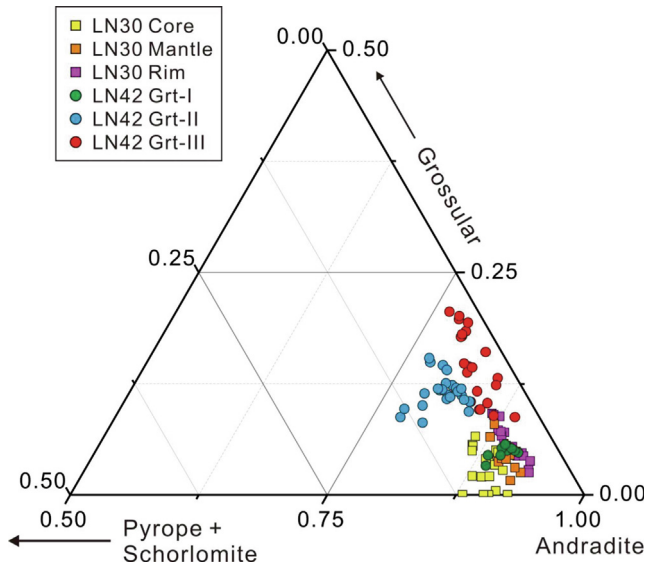

Fig. 6. Ternary diagram showing the variation range of LN30 and LN42 garnet end-member components.

Mg-Ti-Ni-Nb, along with increasing concentrations of Zr-Hf-Yb-Lu from the inner cores to the mantle regions and/or outermost rims. Additionally, their chondrite-normalized REE patterns (Fig. 9A–C) show that these andradites are enriched in light REE (LREE) relative to heavy REE (HREE), and exhibit slightly positive Ce anomalies (δCe: 1.09 – 1.29; on average 1.18) but weakly negative or no Eu anomalies (δEu: 0.82 – 1.10; on average 0.97). Among them, a high percentage of the studied andradites (i.e., LN30 Grt-core and Grt-mantle) display convex-upward to weakly sinusoidal REE patterns (see Fig. 9A and B). The abundances of REEs are characterized by a relative depletion of La compared to the other LREEs, which typically peak at Ce and then gradually decrease from Pr (or Nd) to Ho (or Er), sometimes followed by an increase from Er to Lu (especially in those LN30 Grt-mantle profiles).

Likewise, the LN42 garnet samples were also divided into three groups based on geochemical signatures of major and trace elements. These diverse types of andradites are coincidently in accordance with the three generations of LN42 garnets identified in this study. Overall, a large number of andradite grains are found to have consistently low levels of U varying in a narrow range from 0.49 to 3.85 μg/g (with an average value of 1.56 μg/g), whereas Th concentrations range from 0.64 to 24.30 μg/g (on average 8.08 μg/g) with an average Th/U ratio of 5.28 (N = 43). Moreover, their total REE (ΣREE) concentrations vary from 136.16 to 507.94 μg/g, with an average content of 254.74 μg/g. Chondrite-normalized REE patterns (Fig. 9D–F) show that they are typically enriched in LREEs relative to HREEs, and exhibit weakly negative Ce anomalies (δCe: 0.84 – 0.98; on average 0.89) but variable positive Eu anomalies (δEu: 1.07 – 1.67) with an average of about 1.30. Among them, the oldest generation of LN42 Grt-I xenocrysts are characterized by low Al_2O_3 (<1.3 wt%) but relatively high concentrations of Ti, Zr and LREEs, displaying moderately fractionated REE patterns with gradually increasing Yb and Lu (Fig. 9D). By contrast, the group of LN42 Grt-II titaniferous garnets have elevated levels of Ti, Mg and Al but comparatively lower LREE contents and Th/U ratios, with rather smooth, rightward-inclined REE patterns (Fig. 9E). Notably, the group of corroded or "metasomatized" hydroandradite grains (LN42 Grt-III) are characterized by relatively high Al_2O_3 (up to ~ 4 wt%), but depleted in Mg, Ti, Zr and HREEs (see Fig. 8), with strongly fractionated, LREE-enriched patterns exhibiting remarkable positive Eu anomalies (Fig. 9F).

4.3. U-Pb ages from Kimberlite-hosted garnets

The U-Pb isotopic results along with corresponding U-Th-Pb concentrations of LN30 and LN42 andradites are presented in Supplementary Table S3. Even though it has been proven that the matrix effects and elemental fractionation during LA-ICP-MS analysis of garnet samples can be effectively minimized just by optimizing the laser-ablation parameters or analytical modes (Deng et al., 2017; Fu et al., 2018; Wafforn et al., 2018; Li et al., 2019; Chen et al., 2021; Tang et al., 2021), it is still recommended to use suitable matrix-matched certified reference materials (rather than zircon) as external calibration standards for garnet U-Pb dating (Yang et al., 2018). In addition, garnet U-Pb isotope and trace element analyses affected by U-rich mineral inclusions were excluded during data processing. We also discarded a number of dating results whose time-resolved signals of $^{206}Pb/^{238}U$, $^{207}Pb/^{235}U$ and $^{207}Pb/^{206}Pb$ were disturbed (i.e., deviating from a flat downhole profile), considering that abrupt changes in these ratios highlight the presence of mixed isotopic domains undetected by routine SEM-BSE imaging (especially for some partially replaced or indistinctly zoned grains).

Used as a primary reference material for LA-ICP-MS garnet U-Pb dating, the Mali grandite was sourced from alluvial deposits in southern Mali. It has an average composition of $Adr_{52}Grs_{37}$, with a well-constrained U-Pb age of 202.0 ± 1.2 Ma determined by ID-TIMS (Seman et al., 2017). As listed in Supplementary Table S5, 28 spot analyses of Willsboro andradite yielded a weighted mean $^{206}Pb/^{238}U$ date of 1029.3 ± 9.5 Ma (MSWD = 0.40), which is in excellent agreement with the recommended value (1022 ± 16 Ma) within experimental uncertainties. For LN30 andradite samples (mostly with detectable U, low Th concentrations and Th/U < 5), a total of 29 analytical spots plotted in the

Fig. 5. (A) SEM-BSE image illustrating chemical zoning in some euhedral to subhedral grandite garnet phenocrysts with distinct resorbed inherited cores from the No. 42 pipe. (B) - (D) EPMA-WDS elemental maps showing the distribution of Al, Ti and Fe in typical Grt-II samples associated with magnetite and chlorite/serpentine group minerals hosted by a calcite matrix. Note that their first-nucleated Grt-I cores (only rarely preserved) and later-formed thin growth bands are richer in Fe but depleted in Al relative to the grossular-rich mantle regions, followed by a remarkable Ti increase towards their outermost rims. (E) & (F) Individual Grt-II grain exhibiting an outward diffusional profile of Ti during differentiation of kimberlite melts. As indicated by the color scale, the abundance of Ti is gradually elevated towards the rim. Intracrystalline Ti diffusion has also been observed locally. (G) Some partially replaced remnants of slightly zoned Grt-II with higher proportions of schorlomite-rich component at grain margins, overgrown by infiltration-driven metasomatic reaction domains. (H) - (J) Corroded andradite microcrysts in LN42 kimberlite samples (with high degrees of alteration) are apparently unzoned, mostly free of inclusions and surrounded by groundmass andradite clasts or other accessory mineral phases including fine-grained magnetite, apatite, rutile, titanite as well as sporadic pyrite. This type of garnet (classified as Grt-III) commonly displays porous spongy textures with irregular-shaped or more rounded morphologies, probably originated from the disaggregation of xenocrystic Grt-I precursors caused by later alteration involving partial resorption (dissolution) and replacement reactions. (K) Resorbed atoll-textured spinel, consisting of euhedral titanian-chrome-magnetite core which is isolated from the rim of magnetite-andradite by spongy lagoon phases containing serpentine and/or calcite. (L) Note the presence of silicate-rich globules hosting Grt-I remnants rimmed by thin mantle of groundmass Grt-III clasts or secondary mineral phases (similar in appearance to carbonate segregations or xenoliths with unique nodule-like structures), which is usually considered to be cognate with the host kimberlitic rocks (Ap: apatite; Cc: calcite; Chl: chlorite; Grt: garnet; Mag: magnetite; Py: pyrite; Rt: rutile; Spl: spinel; Srp: serpentine; Ttn: titanite).

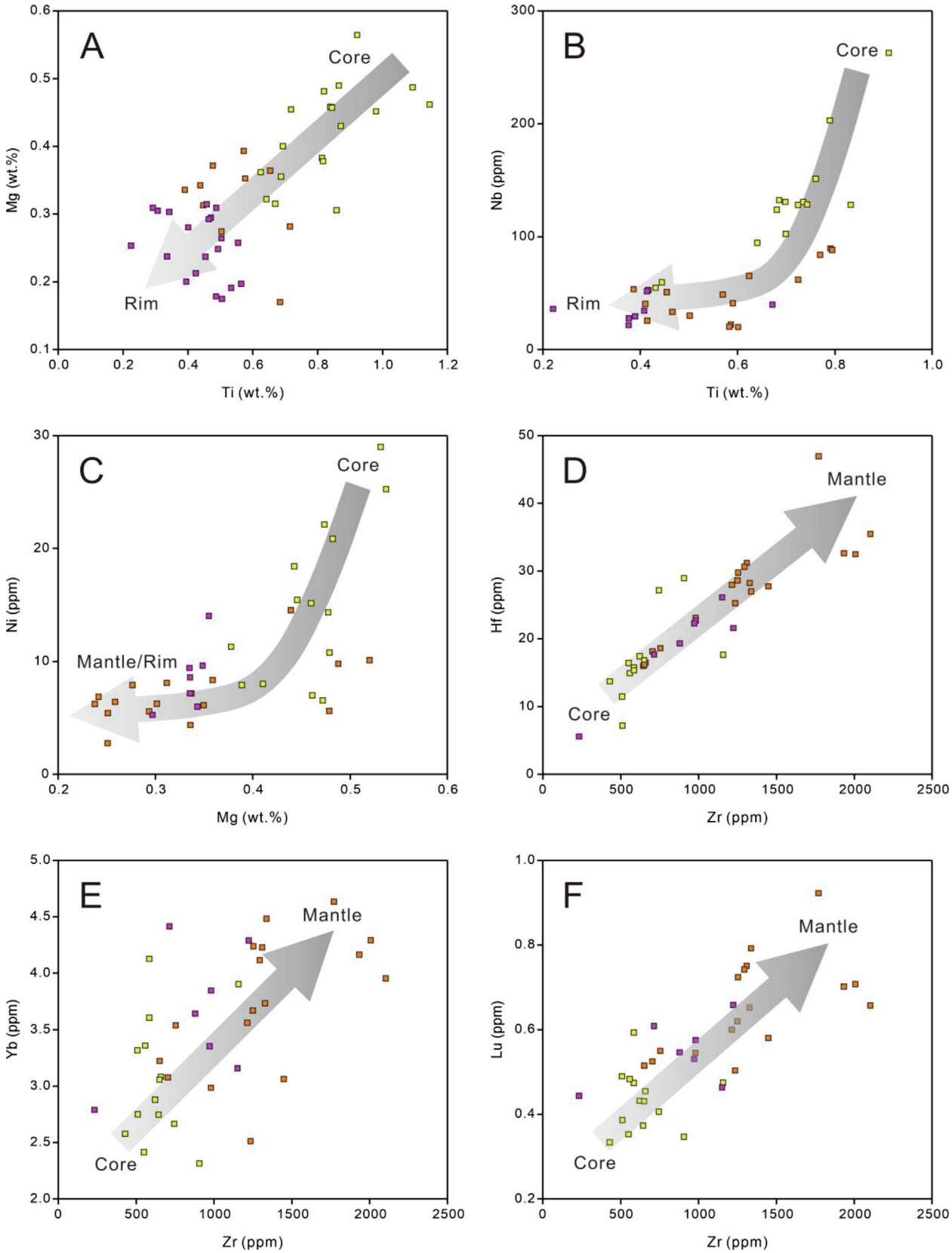

Fig. 7. Geochemical characteristics and compositional evolution of LN30 garnet grains from core to mantle/rim. (A) Ti versus Mg; (B) Ti versus Nb; (C) Mg versus Ni; (D)–(F) Zr is plotted against Hf, Yb and Lu, respectively.

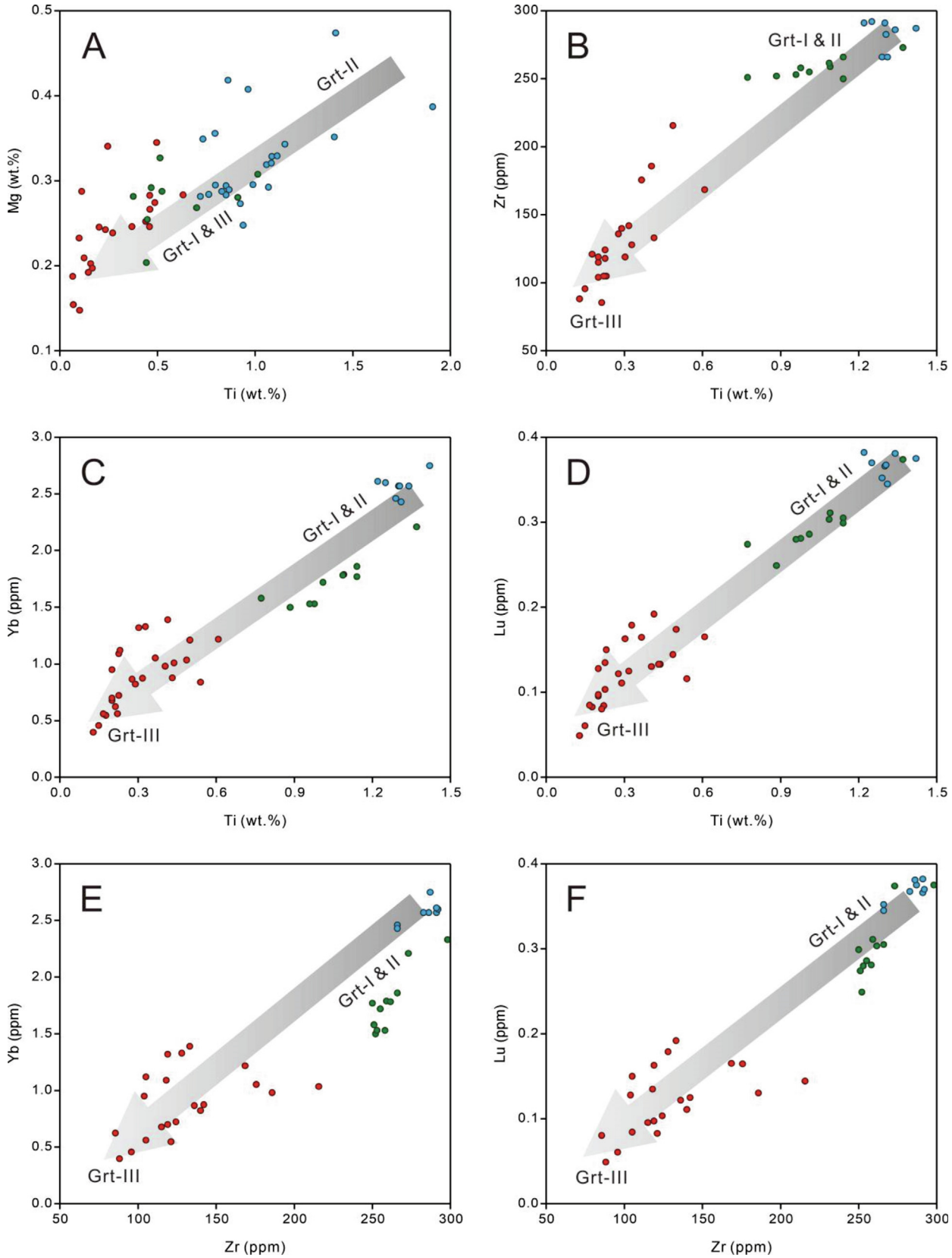

Fig. 8. (A)–(F) Scatter plots showing geochemical variations of selected major and trace element concentrations (Ti-Mg-Zr-Yb-Lu) in different types of LN42 andradite-rich garnet samples based on EPMA/LA-ICP-MS analyses.

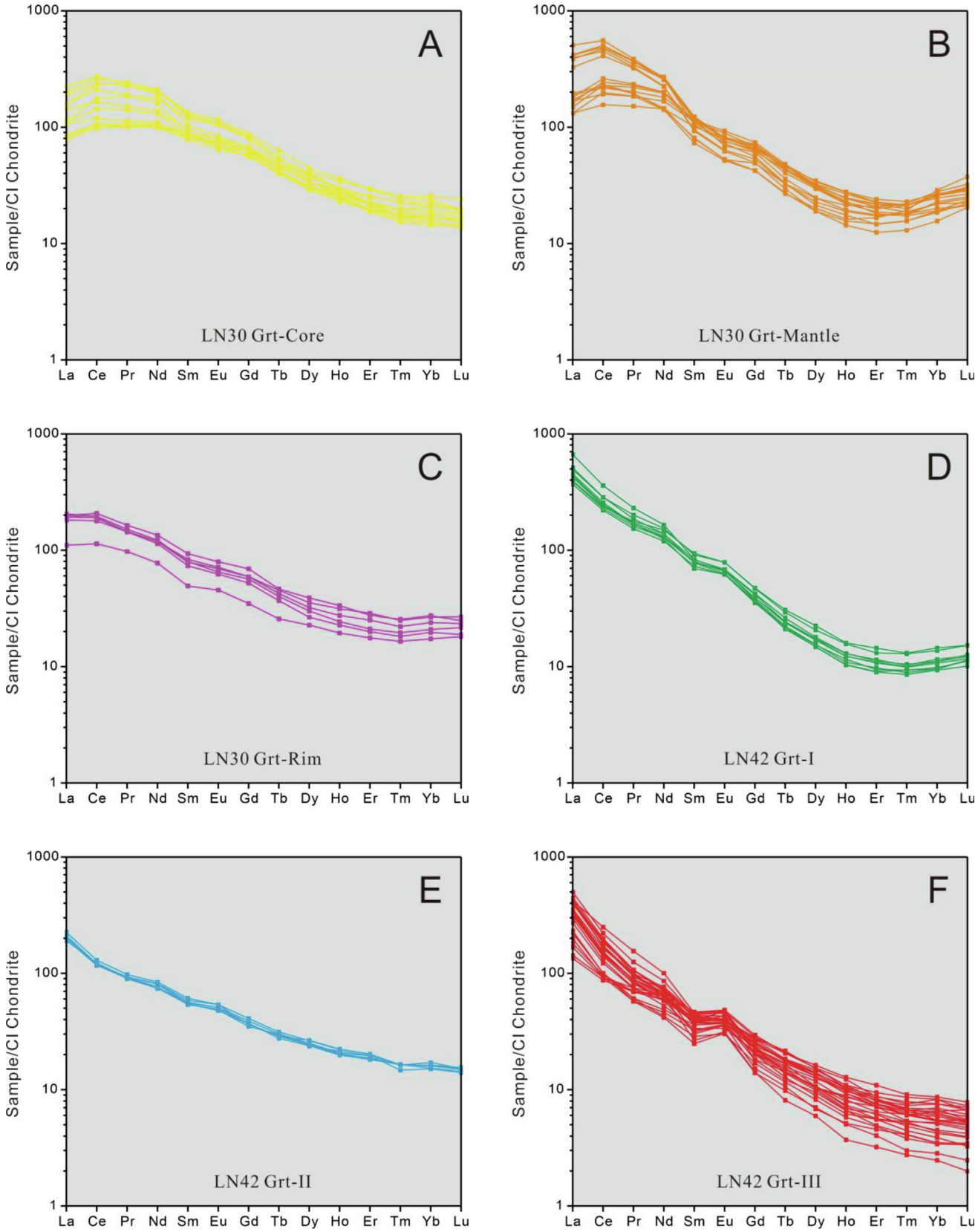

Fig. 9. Chondrite-normalized REE patterns of (A) - (C) LN30 and (D) - (F) LN42 andradite-rich garnet samples from the No. 30 and No. 42 kimberlite pipes. Normalizing values for chondrite are from McDonough and Sun (1995).

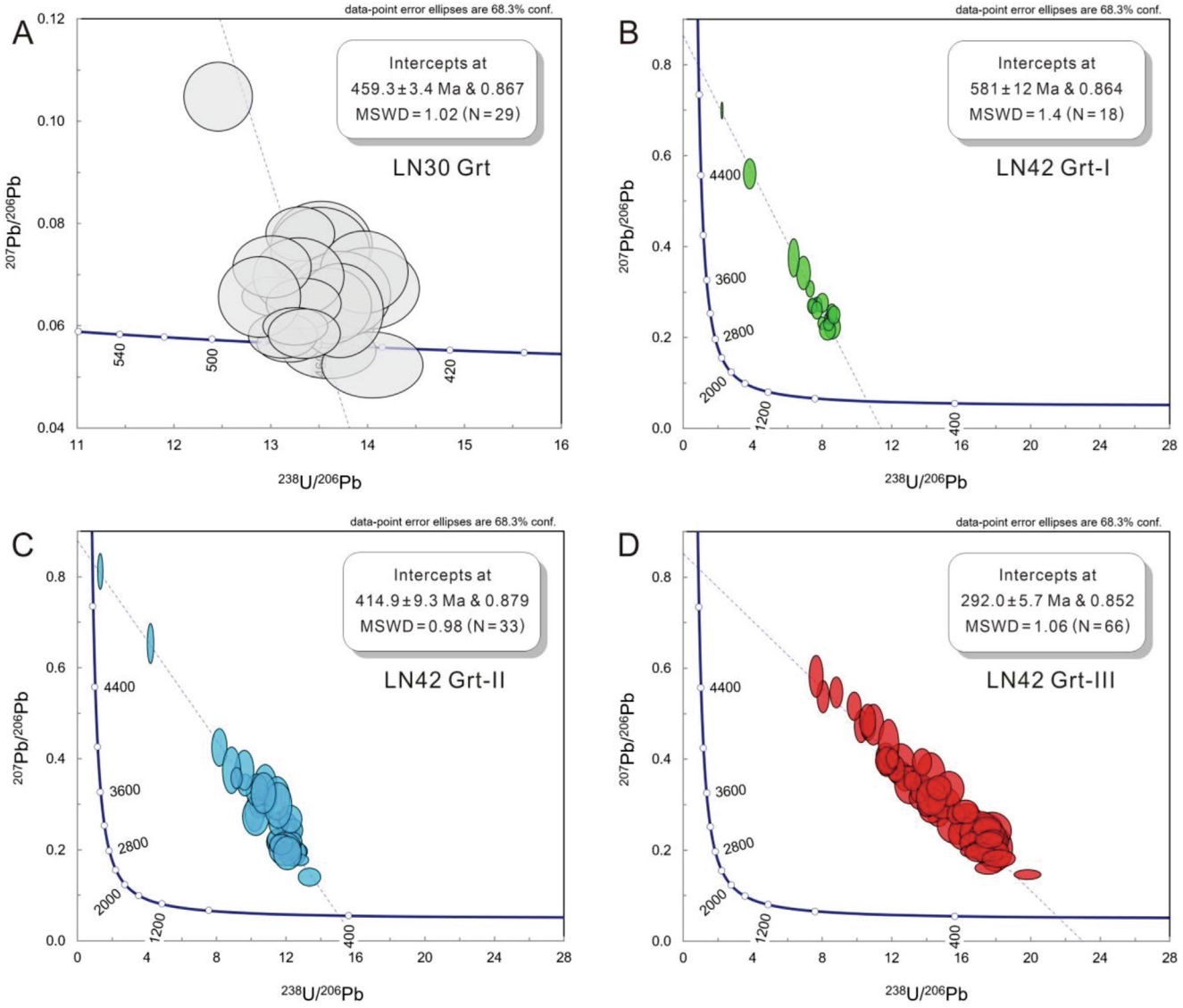

Fig. 10. LA-ICP-MS U-Pb dating results plotted in Tera-Wasserburg concordia diagrams for different types of andradite-rich garnet crystals from the Wafangdian (A) No. 30 and (B)–(D) No. 42 kimberlite pipes. Their lower intercept ages from the T-W plots were calculated using IsoplotR software (Vermeesch, 2018 and references therein).

Tera-Wasserburg concordia diagram were very close to the lower intercept. These uncorrected U-Pb isotope data yielded a nearly concordant age with a large variation of $^{207}Pb/^{235}U$ values owing to their extremely low ^{207}Pb contents and almost negligible common Pb (see Supplementary Table S3). Calibrated by Mali grandite and Willsboro andradite standards, these euhedral to subhedral andradite phenocrysts obtained a lower-intercept $^{206}Pb/^{238}U$ age of 459.3 ± 3.4 Ma (MSWD = 1.02) in the T-W $^{207}Pb/^{206}Pb$ versus $^{238}U/^{206}Pb$ plots (Fig. 10A). The ^{207}Pb correction methods employed in this study have been proposed by Chew et al. (2011), which involves an estimate of the initial Pb isotopic composition (anchored at 0.867) based on the Stacey and Kramers (1975) model for the approximation of terrestrial Pb isotope evolution.

Additionally, the three texturally and compositionally distinct population of LN42 garnet samples (Figs. 6 and 11) define distinct regression lines in the Tera-Wasserburg diagram (Fig. 10B–D) with lower intercept ages of 581 ± 12 Ma (MSWD = 1.4), 414.9 ± 9.3 Ma (MSWD = 0.98) and 292.0 ± 5.7 Ma (MSWD = 1.06), respectively. Strikingly, these significant differences are also reflected in some euhedral- to subhedral-shaped, apparently zoned garnet grains comprising of ancient inherited Grt-I cores and later-formed Ti-rich Grt-II rims with various ages (Fig. 5A), which recorded at least two completely different growth episodes separated by as much as ~ 160 Ma.

4.4. Carbon and oxygen isotopic compositions

Twelve whole-rock/micro-drilled subsamples of calcite-bearing kimberlites from two pipes were analyzed (as presented in Supplementary Table S4), in order to constrain the origin of groundmass carbonate (closely associated with andradite) in terms of stable isotopic signatures. The $\delta^{13}C$ values for bulk carbonate fractions of LN30 and LN42 samples vary from −4.86‰ to −3.68‰ and −7.71‰ to −5.68‰, respectively. Obviously, the majority of them have carbon isotopic compositions comparable to those $\delta^{13}C$ ratios accepted for magmatic calcite in kimberlites, carbonatites and other related rocks, which are well within the distribution range of $\delta^{13}C$ values measured for mantle carbonate phases (Fig. 12). On the other hand, these two sets of kimberlite subsamples in association with carbonate-serpentine segregations have high $\delta^{18}O$ values ranging from 19.19‰ to 20.55‰ and 12.05‰ to 16.00‰, respectively. Such results are much different from each

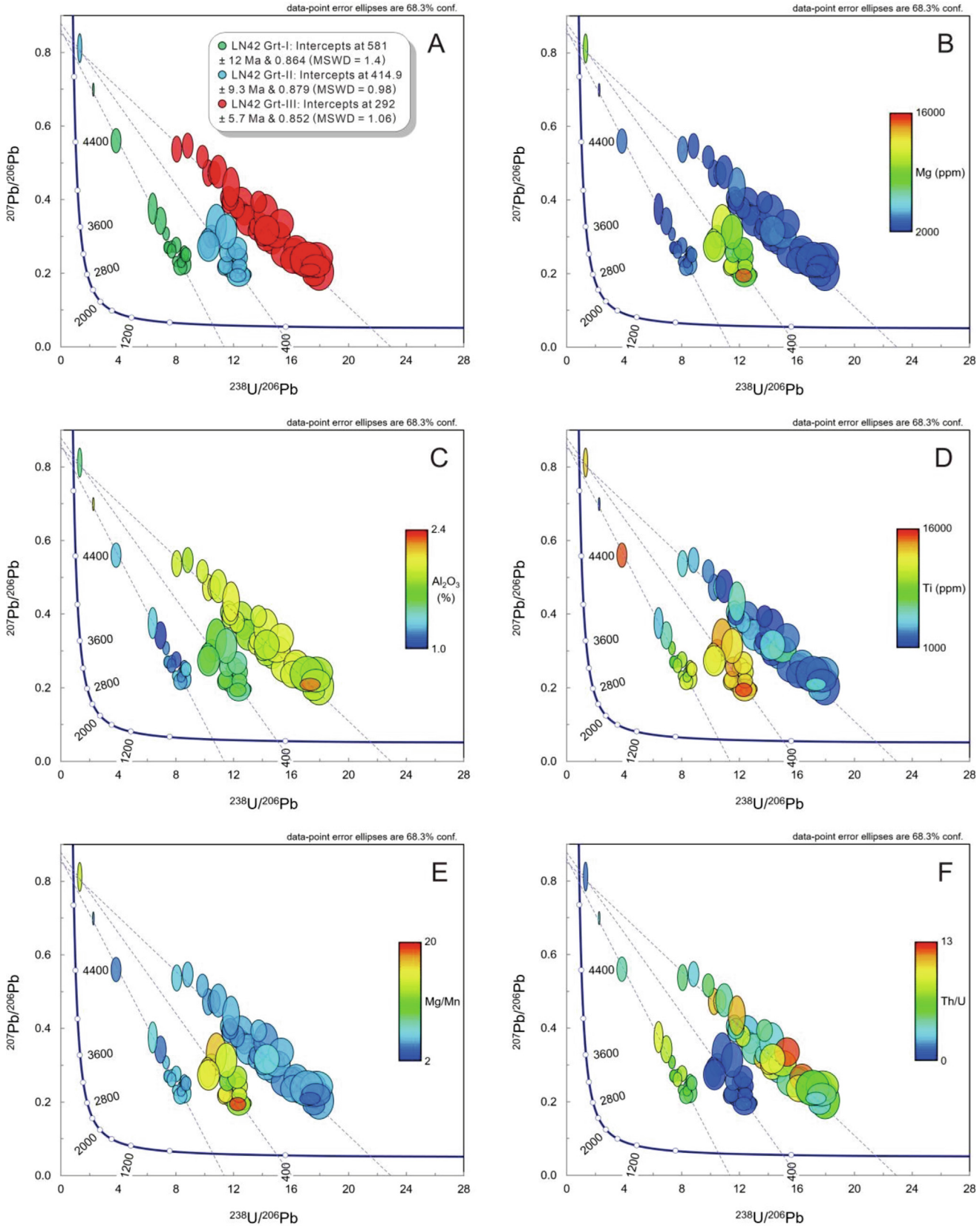

Fig. 11. Compositional diversity among three groups of LN42 garnet data points (in relation to different lower intercept ages shown in the T-W concordia diagram) plotted as color-scale filled error-ellipses using Isoplot 4.15 software (Ludwig, 2012), based on LA-ICP-MS U-Pb isotope data and element concentration results (see Supplementary Table S3).

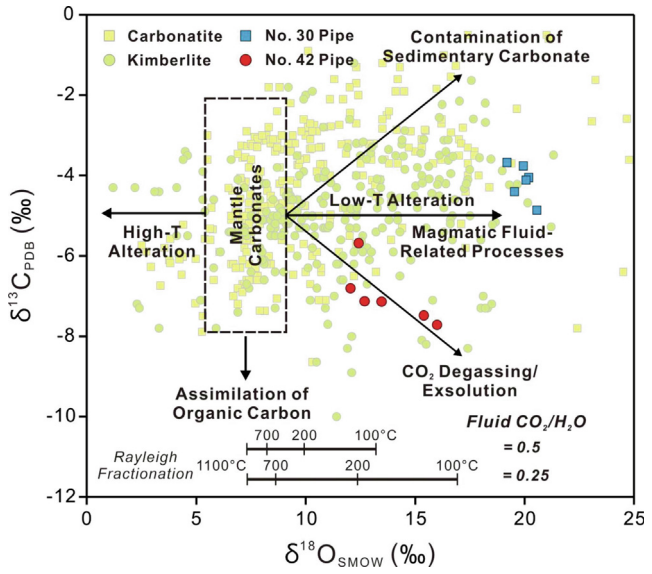

Fig. 12. Schematic $\delta^{13}C$ versus $\delta^{18}O$ (‰ relative to V-PDB and V-SMOW, respectively) diagram for whole-rock carbonate fractions of calcite-bearing kimberlite samples from the Wafangdian No. 30 and No. 42 diamondiferous pipes. Available data for global bulk carbonatites and hypabyssal kimberlites are also shown for comparison, as compiled from published literature sources. See Tappe et al. (2017) and references therein. The "mantle carbonate" box reveals the distribution range of expected $\delta^{13}C$ and $\delta^{18}O$ values for mantle carbonates, modified after Giuliani et al. (2014) and Howarth et al. (2019). As illustrated qualitatively by the arrows, syn-/post-magmatic processes including open-system CO_2-degassing and concomitant Rayleigh fractionation as well as low-temperature alteration related to deuteric fluids could potentially change the stable C—O isotopic compositions of carbonates crystallized from mantle-derived magmas (Deines, 2002, 2004; Wilson et al., 2007). The temperature scales at the bottom refer to two closed-system isotopic fractionation models between primary kimberlitic carbonates and magmatic fluids with variable molar CO_2/H_2O ratios. See Wilson et al. (2007) and Tappe et al. (2008) for more details.

other (with no overlap) and significantly higher than most published analyses of primary carbonates or mantle-derived carbonatitic xenoliths in hypabyssal kimberlites worldwide (Fig. 12).

5. Discussion

5.1. Origin of Carbonates: Primary vs. Secondary

In Wafangdian field, andradite has been encountered as a relatively rare accessory mineral in contrast to subcalcic garnets dominated by pyrope (Zhu et al., 2019b; Ni and Zhu, 2020). However, in LN30 and LN42 samples, the carbonate matrix and silicate-rich globules are both characterized by abundant titaniferous andradites. Calcite, a common mineral phase in these two kimberlite pipes, is often found in a close spatial association with late-stage alteration assemblages, occupying intermediate paragenetic positions between fragmented andradite phenocrysts, serpentinized olivine pseudomorphs, altered phlogopite, chlorite or magnetite grains. In kimberlitic rocks, carbonate minerals are generally considered to be principally of primary magmatic origin or formed from deuteric (i.e., late-stage magmatic) fluids, but some carbonates also crystallized from post-magmatic fluids of external derivation (Mitchell, 1986, 1995; Armstrong et al., 2004; Wilson et al., 2007). Moreover, in cases where kimberlite magmas are emplaced into limestone-rich strata, extensive carbonatization could have resulted from wall-rock assimilation (Armstrong et al., 2004; Wilson et al., 2007; Giuliani et al., 2014). As a result of frequent intense alteration and/or potential contamination by crustal country rocks, it is indeed quite difficult to demonstrate whether the carbonates and related matrix minerals are primary or secondary (Armstrong et al., 2004; Wilson et al., 2007; Hayman et al., 2009; Cheng et al., 2014). Hence, before discussing the origin and timing of andradite-rich garnets in these kimberlite pipes, the effects of carbonatization or low-temperature alteration must be evaluated on the basis of petrographic textures and whole-rock stable isotopic evidence, in order to gain a better understanding of the genesis of calcite-serpentine segregations and silicate-rich globules, as well as their relation to the formation of andradite.

As summarized in Fig. 12, it is evident that primary/unaltered carbonates crystallized from pristine, uncontaminated mantle-derived melts should plot in a restricted $\delta^{18}O$-$\delta^{13}C$ field (Giuliani et al., 2014). Nevertheless, detailed investigations of carbonate phases in kimberlites and carbonatites have revealed a much broader range of $\delta^{18}O$ and $\delta^{13}C$ values. In magmatic systems, the effects of crystal fractionation, degassing of volatiles and the key role of deuteric fluids have been shown to produce certain variations of $\delta^{13}C$ in carbonates from hypabyssal kimberlites (Wilson et al., 2007). Deuteric fluid is a specific type of late-stage, trapped magmatic-hydrothermal fluid derived from the same cooling magma (Mitchell, 1986; Hayman et al., 2009). As mentioned above, these calcite-bearing assemblages are typical of mantle-like $\delta^{13}C$ values measured for kimberlitic carbonates, but have $\delta^{18}O$ values extending towards heavier isotopic compositions (significantly higher than the expected mantle range), which is a common feature of bulk analyses of calcite-rich kimberlites and can be explained by more extensive interaction (crystallization or alteration) of carbonates with late-stage low-temperature fluids rich in exsolved volatile phases (Giuliani et al., 2014, 2017; Howarth et al., 2019). Additionally, there is an apparent co-variation of carbon and oxygen isotopic compositions among a suite of LN42 subsamples (i.e., increasing $\delta^{18}O$ with decreasing $\delta^{13}C$ values, which could have resulted from carbonate crystallization after extensive CO_2 degassing/exsolution), whereas no such correlation has been observed in calcite-rich kimberlites from the No. 30 pipe. But interestingly, higher $\delta^{18}O$ values of LN30 subsamples seem to be generally correlated with increased intensity of whole-rock alteration, and consistent with textural overprint of primary groundmass minerals by late-stage calcite and serpentine with increased modal abundances. Such a shift towards heavier O-isotope composition may also be interpreted as reflecting possible contamination by secondary carbonates from the near-surface sedimentary strata, but their corresponding C-isotope signatures cannot be produced by assimilation of the country rocks (Wilson et al., 2007; Hayman et al., 2009; Giuliani et al., 2014, 2017).

Although the LN30 and LN42 subsamples contain variable amounts of calcite, their bulk $\delta^{13}C$ values are generally consistent with primary mantle-derived carbon (Deines, 2002). However, none of these calcite-bearing kimberlites exhibit mantle-like oxygen isotope compositions (Wilson et al., 2007; Giuliani et al., 2014). All whole-rock carbonate fractions have $\delta^{18}O_{SMOW}$ values > 12‰, i.e., obviously not in equilibrium with mantle peridotite (+5.5‰, data from Mattey et al., 1994). In particular, LN30 calcite-rich samples tend to be even much heavier in oxygen isotopic compositions (typically $\delta^{18}O_{SMOW}$ > 19‰) compared to LN42 kimberlites (Fig. 12). Such a wide range of $\delta^{18}O$ values accompanied by only small variations in $\delta^{13}C$ has been known from primary carbonates in hypabyssal kimberlites, carbonatite dykes and other volatile-rich ultramafic alkaline intrusions (e.g., Tappe et al., 2017 and references therein). Moreover, the abundances of fluid-mobile large-ion lithophile elements (LILEs) show only a restricted range in LN30 kimberlite samples. This excludes the possibility of carbonate O-isotope overprinting by externally-derived meteoric fluids. By contrast, the LILEs behave less coherently in LN42 samples (see Supplementary Table S4). For example, the variabilities of K, Cs, Rb, Sr and Pb (with significant change in bulk rock

composition) suggest that their initial concentrations have been disturbed by low-temperature alteration related to magmatic/deuteric fluids. Previously, Wilson et al. (2007) modeled the closed-system O-isotope fractionation between (kimberlite-hosted) primary carbonates and coexisting magmatic CO_2-H_2O fluids as a function of temperature and fluid CO_2/H_2O ratio, and demonstrated the strong influence of fluid CO_2/H_2O ratios on the range of oxygen isotopic fractionation at temperatures below 750 °C (i.e., along a magmatic cooling path, see temperature scales in Fig. 12). In this model, the calculated $\delta^{18}O$ value of primary magmatic carbonate increases from approximately 7‰ to 17‰ upon cooling over the temperature range of 1100–100 °C, assuming an equilibrium magmatic fluid with a CO_2/H_2O ratio of 0.25 (Wilson et al., 2007; Tappe et al., 2008). The observed range of $\delta^{18}O$ values for LN42 kimberlites are roughly comparable to those modeling results and thus consistent with subsolidus (low-temperature) O-isotope fractionation between mantle-derived carbonates and H_2O-rich magmatic or deuteric fluids with a relatively low molar CO_2/H_2O ratio.

On the other hand, Tappe et al. (2006) suggested that the separation of immiscible carbonatite liquids from rapidly ascending hybrid carbonated silicate magmas at shallow cratonic lithosphere conditions can lead to CO_2 saturation, which can cause carbonate melt segregation and associated CO_2 escape (via near-surface degassing). Likewise, both types of kimberlite rocks also show petrographic evidence of the coexistence of immiscible silicate and carbonatite liquids, such as sub-rounded to rounded carbonate globules/segregations locally present in the silicate-dominated matrix and, more rarely, silicate-rich globules (or irregular patches) associated with late-stage calcite veins cross-cutting the groundmass (see the spatial distribution of mineral phases identified by SEM-based TIMA mapping, as shown in Fig. 3A and 3B). Thus, the distinctively heavier carbon isotopic compositions of LN30 "carbonatite-like" kimberlites might be reproduced by an open-system Rayleigh fractionation process between carbonate-rich residual melts (evolved from kimberlitic parental magmas, with −5‰ $\delta^{13}C$ as guided by the mantle average) and CO_2-rich fluids/volatiles at a range of temperatures from 1100 to 600 °C pertinent to carbonated silicate melt evolution (Tappe et al., 2017). Therefore, we should acknowledge that there might be a possible genetic link between the late-stage kimberlite magmas and coeval carbonatite-like dykes from the Wafangdian field (especially at the No. 30 pipe), probably via fractionation processes involving development of residual carbonate-rich melts/fluids (Sparks et al., 2009; Dongre and Tappe, 2019).

5.2. Origin of Andradite-rich garnets

Andradite-rich garnets are widespread in crustal metamorphic rocks and skarns, which can also be generated (but comparatively rare) in some mantle-related rocks including serpentinized peridotites from ophiolites (Ghosh et al., 2017) and silica-undersaturated alkaline ultramafic complexes (Barrie, 1990; Müntener and Hermann, 1994; Vuorinen et al., 2005; Tappe et al., 2006, 2009; Marks et al., 2008; Dongre et al., 2016; Salnikova et al., 2019; Choudhary et al., 2020; Millonig et al., 2020; Stifeeva et al., 2020). Here, the Wafangdian kimberlites containing abundant andradites pose an interesting problem regarding the nature of these calcic garnets. Despite mantle-derived peridotitic garnet being a common megacryst phase found at the Wafangdian and Mengyin diamond mines, all investigated Ti-andradites are quite distinct from those Cr-pyrope xenocrysts observed by Zhu et al. (2019b) in the same kimberlite pipe. According to a new graphical classification scheme for the discrimination of crust- and mantle-derived low-Cr garnet megacrysts (as proposed by Hardman et al., 2018), the compositions of these kimberlite-hosted, titaniferous andradite phenocrysts demonstrate the proliferation of cratonic crustal garnets in thin sections and hand-picked mineral separates (with most data points plotted in the "crust" field based on a natural logarithmic-scaled Ti/Si versus Mg/Fe bivariate diagram), which may often be misclassified as the "G3" (high-Ca, low-Cr) eclogite suite of mantle origin in terms of a conventionally used Cr_2O_3/CaO discriminatory diagram (Schulze, 2003; Grütter et al., 2004).

In order to understand the primary/magmatic versus non-kimberlitic/xenocrystic origin of Ti-bearing andradites in the Wafangdian kimberlites, the nature of mineral inclusions trapped within garnet phenocrysts and the pressure–temperature conditions of garnet formation, as well as their major-trace element compositions all need to be considered. However, the geochemical characteristics (variation in major and trace elements) of andradite sometimes do not adequately allow for distinguishing between magmatic or metasomatic origin, because compositional constraints might be further complicated by the common alteration of kimberlitic rocks related to post-emplacement fluids of various origin (deuteric/hydrothermal/meteoric) or partially overprinted by secondary processes during magmatic ascent and eruption, owing to the interaction between parental melts and abundant xenoliths entrained from the mantle or crustal rocks (Giuliani et al., 2014). Consequently, the U-Pb ages of andradite garnets from two localities in the Wafangdian field may not be entirely representative of the main episode of Paleozoic kimberlitic magma activity at a regional scale, unless we are able to ascertain their primary or secondary origins.

Here, we present petrographic and textural evidence suggesting that a certain amount of the Wafangdian Ti-bearing andradites may crystallize directly from silica-poor, carbonate-rich residual melts during the final crystallization stages of kimberlitic magmas, especially in some "carbonatite-like" hand specimens collected from the No. 30 pipe. The majority of discrete andradite crystals with smaller grain sizes (<0.5 mm) compared to those of xenocrystic pyrope megacrysts (Zhu et al., 2019b) show euhedral to subhedral morphologies, highly brecciated textures and angular sharp-edged shapes (see Fig. 4), exhibiting signs of strain-induced brittle fragmentation caused by the explosive eruption processes that occurred during kimberlite magma emplacement and pipe formation. Furthermore, short prismatic crystals of unserpentinized olivine and euhedral fine-grained flakes of primary looking fresh phlogopite inclusions were occasionally found in some individual phenocrysts of unaltered andradite (Fig. 4D and 4F). SEM-BSE images show no discernible patchy zoning, recrystallization or overgrowth textures within these andradites, suggesting a single episode of crystal growth (which might not have undergone multi-stage metasomatic reworking by post-magmatic hydrothermal fluids). Therefore, the LN30 andradite-rich garnets, mostly distributed in a calcite-dominated matrix with mantle-like carbon isotope signatures, are believed to have a primary magmatic origin (probably related to the late-stage evolution of kimberlitic melts).

Likewise, some euhedral to subhedral phenocrysts of zoned garnet observed in LN42 hypabyssal kimberlite thin sections are intimately associated with calcite-rich spherical globules or patches. Their unique structures are similar in appearance to carbonate segregations or nodule-like xenoliths (broadly cognate with the host rocks), which have often been reported in the literature (Armstrong et al., 2004; Wilson et al., 2007; Mitchell, 2008; Giuliani et al., 2014; Kamenetsky et al., 2014; Castillo-Oliver et al., 2018) and usually regarded as unequivocal evidence for primary magmatic carbonate + andradite crystallized from kimberlite magma. In other words, the genesis of LN42 Grt-II hosted by carbonate-bearing coalescent spherulites/patches (mainly composed of Sr-rich calcite) can be normally interpreted as a product of carbonate–silicate liquid immiscibility, and thus may offer

crucial clues to understanding kimberlitic melt evolution in the later stage. By contrast, relict xenocrysts (LN42 Grt-I) are typically sub-rounded to rounded or irregular-shaped. Such morphologies suggest that they likely represent corroded fragments of larger discrete grains which had undergone partial resorption (i.e., melting erosion-dissolution processes) and physical abrasion during ascent through the lithosphere. On the other hand, many of the LN42 Grt-III microcrysts have similar anhedral morphologies, probably originated from the disaggregation of xenocrystic Grt-I precursors. As pointed out by previous investigators (e.g., Cheng et al., 2014), only in some special cases, such as carbonatite metasomatism and/or fluid-rock interaction (similar to those in skarn systems) during garnet growth, remnants of altered Grt-I enclosed in the host silicate-rich globules as well as groundmass andradite clasts can be produced by metasomatic processes, according to the following reaction: $3SiO_2 + Fe_2O_3 + 3CaCO_3 = Ca_3Fe_2Si_3O_{12} + 3CO_2\uparrow$. The SiO_2 and Fe_2O_3 (or magnetite) components are derived from the parental magma and spinel, respectively, whereas the $CaCO_3$ components are probably sourced from a suite of calcite-bearing xenoliths or carbonate segregations.

Moreover, Huggins et al. (1977) suggested that natural Ti-andradite might form under conditions of low oxygen fugacity and SiO_2 activity. Likewise, relatively low SiO_2-activity during andradite crystallization in LN42 kimberlite samples is supported by the occurrences of earlier-formed rutile + spinel/titanian-chrome-magnetite + perovskite (only rarely preserved) assemblages. A subsequent increase of SiO_2-activity is evidenced in the presence of numerous accessory minerals characterized by well-developed atoll or corona textures, including spinel + rutile + titanite + magnetite + Ti-andradite adjacent to the andradite-hosting globules in the groundmass (Fig. 5J – 5L). For example, fine-grained microcrysts (<50 μm) of atoll-textured spinel typically consist of euhedral titanian-chrome-magnetite core which is isolated from the rim of magnetite-andradite by spongy lagoon phases containing serpentine and/or calcite. This phenomenon suggests that they formed through the replacement of spinel possibly by interaction with late-stage residual fluids/melts (Dongre et al., 2016; Choudhary et al., 2020). Similarly, anhedral rutile was partially resorbed and mantled by epitaxial growth of titanite or Ti-magnetite/ilmenite corona, which in turn was surrounded by andradite clasts. The crystallizing sequence can be described by the following reaction series: (1) $TiO_2 + SiO_2 + CaCO_3 \rightarrow CaTiSiO_5 + CO_2\uparrow$; (2) $CaTiSiO_5 + Fe_2O_3 + SiO_2 + 2CaCO_3 \rightarrow Ca_3Fe_2TiSi_2O_{12} + 2CO_2\uparrow$ (Vuorinen et al., 2005; Dongre et al., 2016). These textures also indicate an increase in Ca- and Fe-activity during the final crystallization stages of kimberlitic melts. Consequently, crystallization of essentially pure rutile + perovskite + Ti-magnetite requires a rather high initial enrichment in Ca, Fe and Ti coupled with a low activity of silica in the parental magma. A continuous increase in SiO_2-activity with increased fractionation of the evolved magma is manifested by the disappearance of perovskite and elevated Si contents in later-formed titanite/Ti-andradite. After crystallization of Ti-rich Grt-II grains, Ti-activity drops significantly as a consequence of previous depletion through crystallization of the above-mentioned assemblages, resulting in Ti-poor Grt-III andradites. Noteworthily, degassing of CO_2 from the kimberlite magmas appears to play an important role in driving the andradite-forming reactions, which may facilitate further decarbonation reactions and subsequently dissolve more Fe-oxides to produced andradites, accompanied by the development of spongy-like porous textures in coexisting magnetites (see Fig. 5H). A plausible scenario that could account for significant CO_2 removal is that the intrusive kimberlite was a physically open system, thus allowing CO_2 exsolution and removal from the magma. This is exemplified by the $\delta^{13}C$ and $\delta^{18}O$ values of associated carbonate fractions which plot outside the "mantle range" and are more consistent with the C-O isotopic compositions modified by hydrothermal fluids and degassing.

Notably, a large number of pre-existing Grt-II grains have been partially or completely replaced by later-formed Grt-III hydroandradites, which are considered to be deuteric alteration products of pre-existing minerals and result from the circulation of volatile-rich residual fluids generated in the later crystallization stages of post-emplacement cooling magmas (Kaur and Mitchell, 2013). Thus, many fine-grained Grt-III hydroandradites with lower analytical totals (presumably higher amounts of H_2O) represent a low-temperature, low-pressure secondary phase, whereas Grt-I and Grt-II samples are characterized by relatively low amounts of H_2O and probably formed at much higher temperatures (Amthauer and Rossman, 1998). Distinct textures related to the later growth of Grt-III further indicate that LN42 hypabyssal kimberlites have undergone extensive subsolidus deuteric and/or hydrothermal alteration. The actual reaction mechanism leading to the modification of chemical compositions in zoned garnets likely involve both diffusional and infiltration-driven metasomatism through the crystalline phases along external rims and intragranular cavities or cracks assisted by pore fluids. Chemical zoning in euhedral Ti-bearing Grt-II phenocrysts (Fig. 5A–F) probably represents textures that developed at higher temperatures where diffusion-controlled reactions is more effective (until cooling). Replacement of initial assemblages (including Grt-I inherited cores) by hydroandradites along fractures probably suggest that advective transport of materials (driven by fluid infiltration) was the dominant mechanism of Grt-III growth at lower temperature conditions. One surprising observation is that the complete replacement of Grt-II (with grossular-rich mantle and Ti-rich rim) suggests that Al and Ti, normally considered to be immobile, was completely dissolved and subsequently precipitated as relatively Al-rich hydrogarnets.

5.3. Garnet geochemistry as petrogenetic indicators

Garnet is one of the most important indicator minerals in global kimberlites, among which the subcalcic garnet is considered as a powerful and widely used tool for diamond exploration and resource evaluation of kimberlites (Wang et al., 2000; Nowicki et al., 2007; Klein-BenDavid and Pearson, 2009). The geochemical composition of magmatic and xenocrystic garnet has been widely used as an important tool to constrain its crystallization environment, and thus can serve as a potential petrogenetic indicator for diamond exploration or source-rock characterization in provenance studies (e.g., Shimizu and Richardson, 1987; Zhang et al., 2000; Grégoire et al., 2003; Grütter et al., 2004; Shu and Brey, 2015; Salnikova et al., 2019; Zhu et al., 2019b; Shaikh et al., 2020). So far, particular emphasis has been placed on garnet megacrysts from cratonic mantle xenoliths, primarily limited to peridotitic assemblages predominated by a suite of high-Cr, low-Ca pyrope garnets characterized by typical MREE-enriched, bow-shaped patterns with variable degrees of REE fractionation, which are usually interpreted as products of different episodes of lithospheric refertilization and metasomatic processes involving the migration of different melts/fluids (e.g., Schulze, 2003; Grütter et al., 2004; Malkovets et al., 2007; Stachel and Harris, 2008; Lazarov et al., 2009; Pivin et al., 2009; Kargin et al., 2016; Shchukina et al., 2017; Zhu et al., 2019b).

Overall, primary magmatic andradite-schorlomite garnets are comparatively scarce in the groundmass of kimberlites from worldwide occurrences (Mitchell, 1986), which have also been rarely reported in the Wafangdian diamondiferous kimberlites and associated rock suites. Contrary to what was previously thought, such Ti-andradites appear to be rather common in the No. 30 and No. 42 pipes, which are not restricted to hypabyssal-type or massive, poorly sorted kimberlites and fragmental breccias

in the diatremes erupted through Archean crystalline basement of the NCC, but also occur in "carbonatite-like" kimberlite dykes penetrating early to middle Proterozoic strata. Although a number of studies have been carried out on different varieties of Ca–Fe–Ti-rich garnets, the preferential site-specific substitution of Ti and Fe (involving partial replacement of Si) is not yet resolved (Grew, 2013; Samal et al., 2021). In the present study, we have followed the recommendations of Locock (2008) when making stoichiometric calculations (Supplementary Table S1). Unfortunately, the discrimination between primary magmatic and metasomatic andradite-rich garnet is always problematic (Scheibner et al., 2007), due to their similar mineralogical components and major element chemistry (see Fig. 6). Trace element characteristics, particularly with respect to the variations in high field strength elements (HFSEs) and REE-Y distribution patterns, may hold important clues to the physico-chemical environments of garnet growth, and therefore warrant further study to confirm the genesis of these andradites.

Generally speaking, the LN30 andradite specimens are comparatively enriched in Ti, Sr, Y, Zr, Nb, Hf, U, Th and REEs compared to pyrope garnet xenocrysts from the same kimberlite pipe (Zhu et al., 2019b), whereas their major element distribution is fairly homogeneous. As illustrated in Figs. 7 and 9, most of them can be further subdivided into three groups from core to rim, which are slightly zoned with respect to the distribution of REEs and other trace elements. In particular, the variabilities of Mg, Ti and Cr from the interior parts towards the grain margins seem to be more pronounced than the phenomenon of Si-Ca-Fe zoning, even though no discrete cores or rims could be easily distinguished by BSE imaging because of the subtle difference in average atomic number. This implies that specific trace elements may potentially be more sensitive to chemical and thermobarometric changes in the host rocks than major elements. Their compositional evolution trends (shown by the bold arrows in Fig. 7) exhibit continuous decreases in Ti-Ni-Nb, along with increasing concentrations of Yb-Lu and coherent behavior of Zr-Hf from the inner cores to the mantle regions or outermost rims (Fig. 9A−C). LA-ICP-MS data obtained from a few fresh, euhedral andradite phenocrysts show that Cr concentrations in the cores are typically one order of magnitude lower than those in the mantles or rims. This zonation is also featured by an inversion of Yb/Er ratios (in a kind of downward-concave HREE pattern), which vary from < 1 in the cores to > 1 in the mantles and to ~ 1 in the rims throughout these crystals. The spatial distribution of these HREEs in LN30 andradites can be explained in terms of equilibrium closed-system partitioning models for diffusion-controlled crystal growth, following a simple Rayleigh fractionation process (e.g., Otamendi et al., 2002; Scheibner et al., 2007).

To the best of our knowledge, there are surprisingly few well-documented REE geochemical data of kimberlitic andradite available in the published literature up to date, despite of the sporadic but increasingly common occurrences of Ti-andradites discovered in worldwide kimberlite fields and related diamond deposits (e.g., Cheng et al., 2014; Dongre et al., 2016; Shaikh et al., 2017; Dongre and Tappe, 2019; Choudhary et al., 2020; Tappe et al., 2022). Normally, subcalcic garnet megacrysts from the Wafangdian and Mengyin diamondiferous kimberlites are extremely depleted in LREEs and have similar chondrite-normalized REE patterns to those kimberlite-borne peridotitic garnets from other Archean cratons in Siberia and South Africa, except for relatively high enrichment in MREEs and HREEs (Zhang et al., 2000; Zhu et al., 2019b). On the contrary, calcic garnets from the Wafangdian kimberlites are remarkably different and strongly enriched in more incompatible LREEs. Although some investigators have proposed the preferential incorporation of HREEs in Al-rich garnets (such as grossular and pyrope) and LREEs in skarn-related garnets with more Ca–Fe-rich end-member compositions (e.g., Gaspar et al., 2008), little attention has been paid to the origin of such LREE-enriched sinusoidal patterns in kimberlite-hosted, craton-derived andradites. This could be related to an evolving CO_2-rich melt with carbonatitic affinity (probably operating in shallow cratonic lithosphere), which is proven to be effective in introducing CaO, Sr and LREEs (Howarth et al., 2019; Zhu et al., 2019b). Such a notable observation may shed some light on the mechanism responsible for REE fractionation between melts and andradite, thus can help us better understand the chemical behaviors of rare earth elements in kimberlite samples. But this still needs to be investigated in the future.

Another intriguing feature of their REE distribution profiles is the slight depletion of La relative to Ce, Pr and Nd (typically reach maximum at Ce), which display steps and rounded segments for blocks of REEs and differ from smooth continuous curves (see Fig. 9A–C). Such anomalies cannot simply be explained by the different ionic radii of rare earth elements and are generally referred to as the "tetrad effects" of the lanthanides, which have been recognized in highly evolved felsic igneous rocks such as granites and pegmatites (Bau, 1996; Irber, 1999; Jahn et al., 2001). These convex-upward to weakly sinusoidal REE patterns, reported here for the first time in kimberlitic andradites, are virtually identical to those found in a number of silica-undersaturated alkaline volcanic complexes or carbonatite intrusions from China, Canada, Italy, India and other different localities (e.g., Scheibner et al., 2007; Yang et al., 2018; Samal et al., 2021) which have undergone a high degree of fractional crystallization and/or hydrothermal alteration. Additionally, the presence of M−type tetrad effect (La – Nd group) in the studied LN30 garnets is usually attributed to the result of liquid immiscibility in F–Cl-rich silicate melts (Peretyazhko and Savina, 2010), probably suggestive of late-stage crystallization from residual kimberlite magmas enriched in alkali-carbonate and halogen components (Kamenetsky et al., 2007; Abersteiner et al., 2020) prior to the explosive emplacement beneath the Wafangdian region. Therefore, based on the textural evidence and chondrite-normalized REE patterns, the possibility of their primary magmatic nature is undoubtful.

On the other hand, the Ti-rich population of LN42 Grt-II samples, which may also be regarded as kimberlitic garnets, comprise a minor but distinctive group in the Wafangdian No. 42 pipe. They have elevated concentrations of TiO_2 (up to ~ 3.4 wt%) and much lower Th/U ratios (0.47 – 1.70) relative to the other two groups of andradites from the No. 42 pipe (Fig. 11). Similarly, most of the calcite-associated LN30 andradites are also characterized by somewhat lower Th/U ratios (with an average value of 2.17), perhaps because they originated from a carbonatite-like melt/fluid in which carbonates would predominantly form complexes with U but not with Th. Despite the similar geochemical behaviors between U and REEs in garnet lattice, LA-ICP-MS data of U and total REE concentrations exhibited modest heterogeneity, instead of being homogeneously distributed. Noteworthily, the LN30 andradite phenocrysts have higher LREE and lower HREE contents than those in LN42 Grt-II samples associated with groundmass calcite-magnetite assemblages. As discussed in the previous section, a crystallization sequence has been defined by the paragenetic relationship of rutile + titanite + spinel + Ti-magnetite + Ti-andradite. These observations attest to a change in the chemical composition (i.e., Ca-, Fe-, Ti- and SiO_2-activity) of coexisting silicate melts and also confirm a primary magmatic origin for these Ti-andradites. Thus, the LN30 andradites probably crystallized from a more evolved kimberlitic melt with respect to the parental magma of LN42 Ti-andradite.

By comparison, most of the LN42 Grt-I xenocrysts are characterized by sub-rounded to rounded morphologies and decomposition textures (probably resulting from magmatic corrosion or rapid preferential dissolution in melts). They have moderately

fractionated REE patterns with higher LREE when compared to the LN42 Grt-II Ti-andradites (with a somewhat lower degree of REE differentiation), showing similarity to magmatic andradite phenocrysts from the No. 30 kimberlite pipe. Likewise, their REE distribution patterns can also be most simply and effectively explained as arising from Rayleigh fractionation during garnet growth (Otamendi et al., 2002; Scheibner et al., 2007). In some cases, resorbed inherited cores preserved in a few grandite grains are possibly xenocrystic in origin, because an entrainment of older andradite into a juvenile (kimberlitic) magma should lead to resorption or regrowth of the xenocryst. The later-formed overgrowths on relict Grt-I cores are compositionally variable in Al and Fe (see Fig. 5B and D). It appears that these grandite garnets prefer to incorporate Fe over Al at higher temperature and pressure, while an increase of the oxygen fugacity in the melts should favor the incorporation of Fe^{3+} more than Al^{3+} into the octahedral sites (Scheibner et al., 2007). In addition, we have observed an uneven spatial distribution of titanium in individual Grt-II grains with higher proportions of schorlomite. The features of such progressive compositional variations possibly reflect intracrystalline Ti diffusion (Fig. 5F). Interestingly, for those euhedral grandite crystals with chemical zoning, more andradite-rich domains (including Grt-I cores and Grt-II Ti-rich rims) contain detectable levels of U and thus tend to be more favorable for LA-ICP-MS U-Pb dating, whereas measurement attempts in the relatively Al-rich, Fe-poor mantle regions have not been successful. Although it may be attributed to a multi-element coupled substitution mechanism promoting the incorporation of U into andradite lattices (Rák et al., 2011; Guo et al., 2016; Huang et al., 2022), the precise mechanism of U incorporation into grandite garnet still remains insufficiently constrained.

Moreover, there is detailed petrographic and textural evidence to suggest a secondary origin for the Grt-III group samples (mostly hydroandradite) from the No. 42 pipe. Overall, they display various enrichment of LREE and relative HREE depletion with small positive Eu anomalies. By contrast, metamorphic/hydrothermal andradite-grossular garnets found in many skarn-type ore deposits typically have lower REE contents but also exhibit moderately LREE-enriched and HREE-depleted patterns, with a strong positive Eu anomaly (e.g., Gaspar et al., 2008). It has been pointed out that incorporation of REE into garnets are in part controlled by crystal chemistry and mineral growth kinetics (i.e., substitution vs. interstitial solid solution, surface adsorption-occlusion processes, etc.), but largely affected by external factors such as compositions/physico-chemical properties of fluids/melts and host rocks, environmental conditions or metasomatism dynamics (Gaspar et al., 2008; Cheng et al., 2014; Fu et al., 2018; Xiao et al., 2018). Here, we attribute these similarities and distinctions to the different Ca sources, and variable oxygen fugacity of garnet-bearing assemblages. For examples, the REE contents of carbonatitic fluids are much higher than those in limestone wall rocks. Moreover, the presence of chlorite + magnetite in the kimberlite groundmass indicates that these mineral assemblages were formed at relatively high oxygen fugacities during the later stage of magmatic evolution, thus further suggesting that an oxidizing deuteric fluid may account for the negligible Eu anomaly in some relict Grt-I xenocrysts. Under such redox conditions, Eu was most likely to be present as Eu^{3+} and have a similar geochemical behavior to the other REE^{3+}. It is found that the pH values also play an important role in controlling the fractionation of REEs. Eu^{2+} is preferentially partitioned relative to trivalent REEs into an aqueous phase during fluid-rock interactions. Corroded Grt-III hydroandradite clasts (coexisting with pyrite) may have formed under mildly acidic, reducing conditions during late-stage hydrothermal alteration, which would enhance the stability of soluble Eu^{2+}. Since Eu^{2+} has a larger ionic radius and is thought to be easier to be adsorbed by crystal surface or much more likely to substitute into andradite than Eu^{3+}, resulting in positive Eu anomalies (Cheng et al., 2014; Fu et al., 2018). Hence, the trace element patterns of subsequent Grt-III precipitates reflect the progressive chemical evolution of the residual/hydrothermal fluids. Altogether, our findings are indicative of late-stage low-temperature interaction with deuteric fluids and/or post-emplacement hydrothermal alteration which might have been attributed to the formation of secondary Grt-III andradites in the groundmass.

5.4. Emplacement ages of the Wafangdian kimberlites

Kimberlites and related rocks generally contain abundant crustal or mantle xenoliths, and are highly susceptible to weathering (Mitchell, 1986, 1995). Hence, the combined effects of contamination and post-intrusion alteration make it difficult not only for determining the compositions of parental kimberlite magmas, but also the ages of their emplacement (Li et al., 2011). In this case, we obtained a nearly coherent group of 29 data points with apparent concordance and no inheritance from the LN30 andradite samples. Although all investigated grains are slightly zoned with respect to the distribution of REEs from core to rim (which is a consequence of Rayleigh fractionation during garnet growth), they consistently give a lower-intercept $^{206}Pb/^{238}U$ age of 459.3 ± 3.4 Ma (MSWD = 1.02) in the Tera-Wasserburg concordia diagram, with the regression line anchored through an initial $^{207}Pb/^{206}Pb$ value of 0.867 derived from the Stacey and Kramers (1975) terrestrial Pb evolution model. This dating result provides evidence that at least one population of calcic garnets from the No. 30 pipe crystallized shortly before the explosive eruption of kimberlites at ca. 460 Ma, which roughly matches the main episode (480 – 460 Ma) of early Paleozoic kimberlitic magmatism in the North China Craton but is obviously distinguishable from the ~ 480 Ma Pb-Pb age of xenocrystic baddeleyites (Li et al., 2011). Such a relatively young age is expected inasmuch as these primary magmatic andradite phenocrysts are considered to have formed during the late stages of kimberlitic melt evolution, whereas the baddeleyites are probably xenocrysts derived from older mantle materials (Li et al., 2011).

On the other hand, three types of andradite grains from the No. 42 pipe separately define three well-fitted regression lines with distinctly different lower-intercept ages at 581 ± 12 Ma (MSWD = 1.4), 414.9 ± 9.3 Ma (MSWD = 0.98) and 292.0 ± 5.7 Ma (MSWD = 1.06), respectively. As expected, some (relatively low-Al) LN42 Grt-I crystals - here interpreted as relict xenocrysts or "inherited" cores (similar to zircon, but only rarely preserved in the host kimberlites), appear to predate the actual emplacement event and yielded a lower intercept age of ~ 580 Ma (Fig. 10B), considerably older than the other groups of garnets. Unsurprisingly, pre-existing crustal garnet xenocrysts can be entrained in the Wafangdian kimberlite magmas and these may yield ages significantly older than the time of kimberlite emplacement. For those U-rich accessory minerals from kimberlite-borne xenoliths, the amount of episodic Pb loss (i.e., the degree of discordance) depends mostly on the magnitude and duration of lithospheric heating (e.g., thermal perturbation related to mantle upwelling), and effective diffusive radius of individual grain (Schmitz and Bowring, 2003). Except in rare circumstances, they may have re-equilibrated isotopically with the kimberlitic magmas while being caught by the mantle-derived melts. Apparently, this is not the case in our study. Since most Grt-I grains used for dating are fairly large (several hundred microns in size), Pb loss through volume diffusion should be negligible when considering the very slow diffusion rate for Pb in garnet (Mezger et al., 1989, 1991). The relatively short duration of Paleozoic magmatic pulse in this region also demonstrated the

inadequacy of kimberlite entrainment for disturbing xenocrystic andradite U-Pb systematics.

Coincidently, as previously reported by Zheng et al. (2004), the population of metamorphic zircons in mafic xenoliths (garnet granulite formed at a depth of ~ 30 km) from the Wafangdian kimberlites also recorded an episode of growth occurring at ca. 600 Ma (obtained by LA-ICP-MS U-Pb dating), which is generally consistent with our new results. Unfortunately, the growth of Grt-I remains poorly constrained and does not correspond to any well-documented major crustal reworking/underplating event in the eastern NCC (Lu, 2010). However, there is a widespread hiatus in sedimentation, represented by a regional parallel disconformity across large parts of the craton in Late Proterozoic to Early Cambrian time (Piper and Zhang, 1997). This regional anorogenic uplift is believed to reflect a tectonothermal event that affected the lower crust (Zheng et al., 2004), which might be recorded in these cratonic lower crustal garnets. Therefore, the first generation of xenocrystic andradites might be derived from the lower crust in the North China Craton (estimated depth > 30 km) and presumably related to an asthenospheric upwelling in late-Neoproterozoic time (just prior to the onset of Caledonian magmatism/orogeny).

By comparison, LN42 Grt-II samples with higher proportions of grossular and schorlomite are characterized by elevated levels of Ti, Mg and Al but comparatively lower Th/U ratios (Fig. 11), which probably originated from a more evolved magma (enriched in Ca, Fe and Ti coupled with a low activity of SiO_2) during the final crystallization stages of kimberlitic melts. Most of them have been partially replaced by later-formed hydroandradites resulting from infiltration-driven metasomatic reactions. Despite that, selected fresh grains of these titaniferous andradites gave an age of ~ 415 Ma (Fig. 10C). Although somewhat later than the major pulse of early Paleozoic kimberlite magmatic activity in the eastern NCC, such an anomalously young age is roughly in accordance with the punctuated, long-lived emplacement history of No. 42 kimberlite pipe dated by K-Ar and Rb-Sr methods (ca. 463–341 Ma; Dong, 1991), which can still provide minimum age estimates for the most recent pulses of Paleozoic kimberlite magmatism in this study area (perhaps close to but not always overlap the true emplacement age). Strikingly, these LN42 Grt-II Ti-andradites and most of the euhedral- to subhedral-shaped LN30 andradite phenocrysts both have similar morphologies and basically the same (magmatic) origin, but they correspond to two different growth episodes separated by as much as 30 – 50 Ma, highlighting the temporal discrepancies between these two adjacent pipes. Therefore, multiple, discrete episodes (at least two separate events) of kimberlite magmatism that occur over a geologically short time interval or a longer time span (>30 Ma) within a single field seem to be more common than formerly recognized in the Wafangdian and Mengyin regions. Not surprisingly, it has been suggested that even an individual kimberlite pipe can record millions of years of magmatism, much longer than previously thought from the classical viewpoint of a rapid and short-duration emplacement history (Ranger et al., 2018).

Furthermore, sub-rounded to rounded andradite grains from the No. 42 pipe are usually regarded as subsolidus deuteric alteration products of earlier-formed Grt-I and Grt-II crystals, probably resulting from the circulation of residual fluids generated in the later crystallization stages of cooling kimberlite magmas. However, these non-kimberlitic Grt-III andradites define a regression line with a well-constrained lower-intercept age of 292 Ma (Fig. 10D). Such a distinct later occurrence of hydrothermal alteration event should not be interpreted as a consequence of late-magmatic deuteric processes. One would expect that a large fraction of Grt-III samples might have suffered at least some minor degree of post-crystallization Pb loss during later decomposition and dissolution-replacement, which could produce misleading U-Pb dating results. Obviously, neither a strong discordance of the data nor a large scatter of ages has been observed in this case, since analyses affected by partial Pb loss might cause a shift of these data points towards higher $^{238}U/^{206}Pb$ values (Millonig et al., 2020). Although a few andradite separates have undergone different levels of alteration, they only suffered minimal loss of radiogenic Pb and did not exhibit any visible disturbance in their U-Pb systems, thus indicating that garnet is as highly resistant to isotopic modification as previously thought (Burton et al., 1995). Even though some xenocrystic andradites may be derived from deep levels of the lower crust (estimated depth > 30 km) and predate the actual emplacement event, many of them can still retain their original age information during residence in the host kimberlitic magma, owing to high closure temperatures (over 850 °C) for U and Pb gain or loss (Mezger et al., 1989). Because of these features, andradites remain stable throughout a wide range of pressure–temperature conditions. Diffusion of U or Pb associated with post-emplacement tectonothermal events can also be considered negligible.

Hence, the relatively younger age obtained from secondary Grt-III andradites is still geologically meaningful and basically represent the time of crystallization, which can help to constrain the timing of post-magmatic regional hydrothermal alteration. This considerably younger population of andradite appears to represent another episode of new hydrogarnet growth, involving the breakdown of precursor andradites. Regardless of whether the andradite-breakdown process involved pre-292 Ma deuteric alteration or subsequent overprinting by intense hydrothermal activity, these Grt-III samples must have been formed at a shallow crustal level under low-temperature, low-pressure conditions. Surprisingly, although the Wafangdian hypabyssal kimberlites have long been strongly affected by metasomatism after emplacement (Tompkins et al., 1998), this late-stage alteration event seems to have little influence on those andradites from the No. 30 pipe (situated approximately 6 km apart from the No. 42 pipe), probably due to various extents of spatial heterogeneity in regional metasomatism, metamorphism and deformation. As revealed by both sampling sites at the local scale (Fig. 2), secondary splay faults off a larger structure of the Tan-Lu fracture zone are considered to exert tectonic controls on near-surface emplacement of these kimberlite pipes in Wafangdian (Dong, 1991). Locally, reactions of the intrusive kimberlites with the surrounding limestone host rocks may have produced more pervasive (small-scale) post-emplacement hydrothermal alteration in the vicinity of No. 42 pipe, resulting in remobilization of sulfides and secondary carbonates from the country rocks into the kimberlite intrusions (Tompkins et al., 1998) as well as extensive dissolution and replacement of pre-existing microcrysts.

5.5. Evaluation of kimberlite geochronometers

Obtaining robust emplacement ages for kimberlites is commonly complicated, not only because they are heterogeneous hybrid rocks consisting of both magmatic and xenocrystic (crustal or mantle-derived) components (Mitchell et al., 2019), but also because kimberlites are readily altered by syn- and post-emplacement interaction with hydrothermal fluids (Giuliani et al., 2017). Conventional Rb-Sr and Ar-Ar (or K-Ar) isotopic methods have long been used to determine the emplacement ages of kimberlite and other alkaline intrusive rocks (Heaman et al., 2019). Generally speaking, the Rb-Sr isochron dates for whole rocks plus selected minerals (consisting of phlogopite, serpentinized olivine and garnet phenocrysts) are older than the ages determined from the phlogopite and perovskite, further illustrating the inhomogeneous hybrid nature of representative bulk kimberlite samples from the North China Craton (Lu et al., 1998).

Previous geochronological studies of the Wafangdian kimberlite pipes have largely focused on phlogopite macrocrysts (e.g., Dobbs et al., 1991; Li et al., 2005; Zhang and Yang, 2007). Both magmatic and xenocrystic mica can be utilized to yield reproducible Rb-Sr and Ar-Ar emplacement ages for many (but not all) kimberlites, regardless of the compositional diversity and often enigmatic origins of kimberlitic micas. The utilization of macrocrystic mica to obtain reliable emplacement ages rests on the relatively low closure temperature (~400 °C) of the Rb-Sr isotopic system in phlogopite (Willigers et al., 2004). This implies that any mantle-derived xenocrystic/antecrystic phlogopite grains are expected to be "reset" upon entrainment in the ascending kimberlite magma and thus should then record the kimberlite eruption age. Except in rare circumstances, it is possible that xenocrystic components from crustal or mantle xenoliths may have their Rb-Sr system only partially reset upon entrainment (e.g., Dalton et al., 2020).

Despite the presence of groundmass phlogopite in kimberlites worldwide, macrocrystic phlogopite is not ubiquitous or abundant in some of the Wafangdian pipes as demonstrated by its paucity in LN30 and LN42 samples from this study. In fact, the majority of kimberlitic phlogopite grains extracted from the No. 30 and No. 42 pipes are usually altered, either by deuteric processes or by post-magmatic chemical weathering (or both). Furthermore, the generally ubiquitous occurrence of carbonates in the Wafangdian kimberlites may pose a serious analytical problem. Typically, kimberlitic carbonates or carbonatites have very high Sr contents and low initial $^{87}Sr/^{86}Sr$ ratios (e.g., Castillo-Oliver et al., 2018; Dongre and Tappe, 2019). Hence, the incorporation of small amounts of "exotic" carbonate in the phlogopite samples could effectively lower the measured $^{87}Sr/^{86}Sr$ and $^{87}Rb/^{86}Sr$ ratios by adding relatively large amounts of common Sr to the system (thus can cause systematic errors in isochron calculations). One can expect that such "isochrons" may be mixing lines between a pure phlogopite end-member and Sr-bearing carbonate contaminant, which will only have true age significance if the phlogopite and coexisting carbonate phases are both primary components of the host kimberlite (Brown et al., 1989). Although some authors used only fresh, relatively unaltered phlogopite megacrysts from the adjacent No. 50 pipe (Zhang and Yang, 2007), the initial $^{87}Sr/^{86}Sr$ values of 0.722 calculated from the phlogopite Rb-Sr isochron regression is much higher than those of the mantle-derived magmas, implying potential complications from crustal contamination and/or later alteration (Li et al., 2005, 2011). In some cases, mixture of different mineral impurities or partial Ar loss was also noticed (Zhang and Yang, 2007). Therefore, phlogopite might not be the most preferable mineral for dating these two kimberlite pipes because of its close relationship with complicated alteration and contamination processes.

In regard to other suitable dating minerals, some authors successfully obtained a ^{207}Pb-^{206}Pb age of 479.6 ± 4.9 Ma from the Wafangdian kimberlite-hosted baddeleyite grains, indicating that early Paleozoic kimberlites in the NCC were emplaced at ~ 480 Ma (Li et al., 2011). Even though dating baddeleyite can yield a precise crystallization age representing the time of regional magmatism, it is rarely found in kimberlites and commonly interpreted as xenocrysts originally formed in deep-sourced melts during metasomatism, which may be inherited from the subcontinental lithospheric mantle (SCLM) or partially assimilated with crustal rocks (but did not crystallize directly from the kimberlitic magmas). Generally speaking, U-Pb dating results obtained from mantle zircon and baddeleyite may be older than the emplacement ages of kimberlitic intrusions because neither of them is a groundmass mineral, but both occur as xenocrysts in kimberlites (Batumike et al., 2008; Heaman et al., 2019).

By contrast, perovskite usually occurs in the kimberlite groundmass and is considered as the best candidate mineral for dating kimberlite, particularly using *in-situ* techniques (such as SIMS and LA-ICP-MS) that can effectively avoid alteration zones or other U-rich inclusions in some crystals, thus providing a robust constraint on the emplacement ages of kimberlites (e.g., Batumike et al., 2008; Yang et al., 2009; Li et al., 2011; Donnelly et al., 2012; Griffin et al., 2014; Tappe et al., 2018b). Unfortunately, despite repeated attempts by means of heavy liquids and hand picking, a clean separation of perovskite from the Wafangdian "carbonatite-like" kimberlite hand specimens was unsuccessful. A possible explanation for its absence in LN30 samples is that perovskite is known to be crystallized as an early liquidus (or near-liquidus) phase from a carbonate-rich kimberlite magma prior to carbonate–silicate liquid immiscibility. Alternatively, the inherently fine grain size of groundmass perovskite also raises challenges for mineral separation.

In comparison with perovskite, andradite-rich garnet is frequently found in the heavy-mineral concentrates of cratonic kimberlites and also more easily separated from crushed materials owing to its relatively large grain size. Although direct dating of calcic garnet varieties from kimberlite pipes has rarely been attempted, such Ti-andradites have been proven to faithfully record the emplacement ages of compositionally diverse magmas (e.g., ultramafic-alkaline and/or carbonatitic intrusive rocks: Salnikova et al., 2018a, 2018b, 2019; Yang et al., 2018; Stifeeva et al., 2020) as its U-Pb isotopic clock would be triggered during magmatic ascent. Moreover, the chemical composition and textural features of different garnet generations can provide some key information about multiple stages of magmatic crystallization or metasomatic alteration associated with kimberlite formation (e.g., Dongre et al., 2016; Zhu et al., 2019b; Choudhary et al., 2020). Therefore, most attention has been focused on kimberlite-hosted andradite in this study.

At the same time, we must admit that Cr-pyrope garnet megacrysts (classified into the well-defined "G9" category) from the more common peridotite suite would certainly be useful to constrain the evolution of mantle metasomatism beneath the North China Craton (Zhu et al., 2019b). However, such extremely low-U samples (mostly < 0.05 ppm or even below detection limits) are found to be less preferable for *in-situ* U-Pb dating using traditional LA-ICP-MS techniques. Therefore, we consider the Wafangdian andradite xenocryst population, especially the LN42 Grt-I samples, as an adequate proxy for lower crustal xenolith materials, which can provide some key (geochronology and geochemistry) information to constrain the tectonothermal evolution of ancient cratonic lithosphere sampled by these kimberlitic rocks and to understand the timing of deep crustal metamorphism or asthenospheric upwelling beneath the North China Craton.

Furthermore, considering that this dating method might be subjected to specific limitations (i.e., a certain texture type of andradite-rich garnet preferred for U-Pb dating), it is necessary to make an assessment of alteration for selected andradite grains before conducting U-Pb analyses in order to obtain precise age data. For example, it is important to examine multiple grains of andradite from the Wafangdian kimberlite field to verify its compositional homogeneity, because it is not unusual for intrusive kimberlite rocks to contain more than one generation of andradites representing distinct and temporally disconnected evolutionary processes. It should also be pointed out that the absence of a clear petrogenetic framework may lead to unknowingly poor spot-selection during *in-situ* analyses for garnet geochronology or trace element geochemistry, and thus would result in erroneous interpretations of our U-Pb data. Thus, careful petrogenetic assessments using a combination of SEM-BSE observation and EPMA-WDS spot analysis (or elemental mapping), perhaps aided by micro-XRF mapping and TIMA scanning, should be considered a prerequisite step to elucidate the complex evolution history of various garnet

types and properly characterize these kimberlite-hosted grains for LA-ICP-MS U-Pb dating.

Last be not least, it would be better to make a comparison of garnet U-Pb dating results with other independent age constraints to assess the validity and reliability of our new geochronological data. For example, a slightly younger age (459.3 ± 3.4 Ma) given in this study is still similar to the previously reported ages within a range of acceptable errors (e.g., Dobbs et al., 1991: 461.7 ± 4.8 Ma; Li et al., 2005: 463 ± 7 Ma; Zhang and Yang, 2007: 463.9 ± 0.9 Ma). Overall, there is good agreement between andradite U-Pb (No. 30 pipe), single-grain mica Rb-Sr isochron and macrocrystic phlogopite $^{40}Ar/^{39}Ar$ dating (No. 50 pipe), which indicates that the above three geochronometers can provide robust age constraints for the emplacement of diamondiferous kimberlites in some cases.

6. Conclusions

Recent analytical developments and availability of matrix-match standards have made garnet more accessible to *in-situ* U-Pb dating by LA-ICP-MS. Advances in the present study led to the awareness that andradite samples recovered from two adjacent kimberlite pipes might belong to different generations issuing from complex diverse evolutionary histories. In this study, kimberlite-hosted calcic garnets identified from the Wafangdian diamond deposit are dominated by andradite with variable but relatively low proportions of schorlomite, grossular and pyrope, overwhelmingly belong to craton-derived crustal garnets. These Cr-poor andradite grains are enriched in Ti, Sr, Zr, Nb, Hf and LREEs compared to previously reported Cr-pyrope xenocrysts from the same study area.

Abundant highly fragmented andradite phenocrysts from the No. 30 pipe yield a lower intercept U-Pb age of 459.3 ± 3.4 Ma, representing a crystallization age coeval with an explosive eruption event of the No. 30 pipe. This date is generally consistent with the main episode (480–460 Ma) of early Paleozoic kimberlitic magmatism in the eastern North China Craton, and thus provides a reliable alternative for the timing of kimberlite emplacement. Their trace element signatures, morphologies and included mineral assemblages suggest a primary magmatic origin linked to carbonate-rich residual melts, probably indicating the very final stage of kimberlite ascent to the diatreme root zones (i.e., at a relatively shallow depth beneath the Wafangdian region).

Calcic garnets from the No. 42 pipe can be subdivided into three distinct types based on occurrence modes, chemical compositions (including REE distribution and zoning patterns) and textural evidence. U-Pb dates from selected titaniferous andradites unravel their multi-stage growth episodes. Among them, resorbed Grt-I crystals yielded a considerably older age of 581 ± 12 Ma, predating the actual emplacement event. These relict andradite xenocrysts might be derived from the lower crust in the NCC, presumably related to an asthenospheric upwelling in late-Neoproterozoic time. By contrast, Grt-II Ti-andradites with elevated Ti, Mg and Al but comparatively lower Th/U ratios gave a relatively young age of 414.9 ± 9.3 Ma, suggesting that at least two discrete episodes of kimberlite magmatism might occur over a geologically short time interval within a single field. Secondary Grt-III corroded hydroandradites yielded an anomalously young age of 292.0 ± 5.7 Ma, indicating that they probably formed during a post-emplacement alteration event (originated from the disaggregation of pre-existing andradites). Their LREE-enriched patterns with a distinct positive Eu anomaly are similar to those of skarn-related grandites, testifying to the active role of later regional metasomatic processes involving low-temperature deuteric/hydrothermal fluids.

CRediT authorship contribution statement

Xiaoming Sun: Investigation.

Declaration of Competing Interest

The authors declare that they have no known competing financial interests or personal relationships that could have appeared to influence the work reported in this paper.

Acknowledgements

This research project was jointly supported by the National Key Research and Development Program of China (Grant Nos. 2018YFA0702605 & 2018YFC0309902), National Natural Science Foundation of China (Grant Nos. 91855213, 42072084 & 41702066), Guangdong Basic and Applied Basic Research Foundation (2019A1515011922), and the Fundamental Research Funds for Central Universities (Nos. 20lgpy64 & 12lgjc05). We thank Dr. Han Zhang as well as the staff of Yanduzhongshi Geological Analysis Laboratories Ltd. (Beijing) for their thoughtful advice and excellent technical support during garnet U-Pb dating and trace element analysis by LA-ICP-MS. We are also grateful to Dr. Can Rao from Zhejiang University for his great assistance with EPMA measurements. In particular, we are deeply indebted to Dr. Haoyang Zhou for many beneficial discussions that ensued during this study. Finally, we sincerely thank Associate Editor Dr. Sebastian Tappe and the reviewer Dr. Leo J. Millonig for their valuable comments, constructive suggestions and great patience, which were really helpful to improve the quality of this manuscript.

Appendix A. Supplementary material

Supplementary data to this article can be found online at https://doi.org/10.1016/j.gr.2022.05.016.

References

Abersteiner, A., Kamenetsky, V.S., Goemann, K., Kjarsgaard, B.A., Fedortchouk, Y., Ehrig, K., Kamenetsky, M., 2020. Evolution of kimberlite magmas in the crust: a case study of groundmass and mineral-hosted inclusions in the Mark kimberlite (Lac de Gras, Canada). Lithos 372-373, 105690.

Agashev, A.M., Orihashi, Y., Pokhilenko, N.P., Serov, I.V., Tolstov, A.V., Nakai, S., 2016. Age of Mirny field kimberlites (Siberia) and application of rutile and titanite for U-Pb dating of kimberlite emplacement by LA-ICP-MS. Geochem. J. 50 (5), 431–438.

Amthauer, G., Rossman, G.R., 1998. The hydrous component in andradite garnet. Am. Mineral. 83 (7-8), 835–840.

Armstrong, J.P., Wilson, M., Barnett, R.L., Nowicki, T., Kjarsgaard, B.A., 2004. Mineralogy of primary carbonate-bearing hypabyssal kimberlite, Lac de Gras, Slave Province, Northwest Territories, Canada. Lithos 76 (1-4), 415–433.

Barrie, C.T., 1990. U-Pb garnet and titanite age for the Bristol Township lamprophyre suite, western Abitibi Subprovince. Canada. Can. J. Earth Sci. 27 (11), 1451–1456.

Batumike, J., Griffin, W., Belousova, E., Pearson, N., Oreilly, S., Shee, S., 2008. LAM-ICPMS U-Pb dating of kimberlitic perovskite: Eocene-Oligocene kimberlites from the Kundelungu Plateau, D.R. Congo. Earth Planet. Sci. Lett. 267 (3-4), 609–619.

Baxter, E.F., Scherer, E.E., 2013. Garnet geochronology: timekeeper of tectonometamorphic processes. Elements 9 (6), 433–438.

Brown, R.W., Allsoppl, H.L., Bristow, J.W., Smith, C.B., 1989. Improved precision of Rb-Sr dating of kimberlitic micas: an assessment of a leaching technique. Chem. Geol. 79 (2), 125–136.

Burton, K.W., Kohn, M.J., Cohen, A.S., Keith O'Nions, R., 1995. The relative diffusion of Pb, Nd, Sr and O in garnet. Earth Planet. Sci. Lett. 133 (1-2), 199–211.

Castillo-Oliver, M., Giuliani, A., Griffin, W.L., O'Reilly, S.Y., 2018. Characterisation of primary and secondary carbonates in hypabyssal kimberlites: an integrated compositional and Sr-isotopic approach. Miner. Petrol. 112 (S2), 555–567.

Chen, Y.-H., Hu, R.-Z., Lan, T.-G., Wang, H., Tang, Y.-W., Yang, Y.-H., Tian, Z.-D., Ulrich, T., 2021. Precise U-Pb dating of grandite garnets by LA-ICP-MS: assessing ablation behaviors under matrix-matched and non-matrix-matched conditions and applications to various skarn deposits. Chem. Geol. 572, 120198.

Cheng, Z., Zhang, Z., Santosh, M., Hou, T., Zhang, D., 2014. Carbonate- and silicate-rich globules in the kimberlitic rocks of northwestern Tarim large igneous province, NW China: evidence for carbonated mantle source. J. Asian Earth Sci. 95, 114–135.
Chew, D.M., Sylvester, P.J., Tubrett, M.N., 2011. U-Pb and Th-Pb dating of apatite by LA-ICPMS. Chem. Geol. 280 (1-2), 200–216.
Chew, D.M., Petrus, J.A., Kamber, B.S., 2014. U-Pb LA-ICPMS dating using accessory mineral standards with variable common Pb. Chem. Geol. 363, 185–199.
Choudhary, B.R., Santosh, M., Ravi, S., Babu, E.V.S.S.K., 2020. Spinel and Ti-rich schorlomite from the Wajrakarur kimberlites, southern India: implications for metasomatism, diamond potential and orangeite lineage. Ore Geol. Rev. 126, 103727.
Dalton, H., Giuliani, A., Phillips, D., Hergt, J., Maas, R., Matchan, E., Woodhead, J., O'Brien, H., 2020. A comparison of geochronological methods commonly applied to kimberlites and related rocks: three case studies from Finland. Chem. Geol. 558, 119899.
Deines, P., 2002. The carbon isotope geochemistry of mantle xenoliths. Earth-Sci. Rev. 58 (3-4), 247–278.
Deines, P., 2004. Carbon isotope effects in carbonate systems. Geochim. Cosmochim. Acta 68 (12), 2659–2679.
Deng, X.D., Li, J.W., Luo, T., Wang, H.Q., 2017. Dating magmatic and hydrothermal processes using andradite-rich garnet U-Pb geochronometry. Contrib. Mineral. Petrol. 172, 71.
Dobbs, P.N., Duncan, D.J., Hu, S., Shee, S.R., Colgan, E.A., Brown, M.A., Smith, C.B., Allsopp, H.L., 1991. The geology of the Mengyin kimberlites, Shandong, China. Int. Kimberlite Conf.: Extended Abstracts 5, 76–78.
Dong, Z., 1991. Some geological characteristics of kimberlite-type diamond deposits in China and their ore-prospecting indicators. Mineral Deposits 10, 255–264. in Chinese with English abstract.
Dongre, A.N., Viljoen, K.S., Rao, N.V.C., Gucsik, A., 2016. Origin of Ti-rich garnets in the groundmass of Wajrakarur field kimberlites, southern India: insights from EPMA and Raman spectroscopy. Miner. Petrol. 110 (2-3), 295–307.
Dongre, A., Tappe, S., 2019. Kimberlite and carbonatite dykes within the Premier diatreme root (Cullinan Diamond Mine, South Africa): New insights to mineralogical-genetic classifications and magma CO_2 degassing. Lithos 338–339, 155–173.
Donnelly, C.L., Griffin, W.L., Yang, J.H., O'Reilly, S.Y., Li, Q.L., Pearson, N.J., Li, X.H., 2012. *In situ* U-Pb dating and Sr-Nd isotopic analysis of perovskite: constraints on the age and petrogenesis of the Kuruman Kimberlite Province, Kaapvaal Craton, South Africa. J. Petrol. 53, 2497–2522.
Duchêne, S., Blichert-Toft, J., Luais, B., Télouk, P., Lardeaux, J.-M., Albarède, F., 1997. The Lu-Hf dating of garnets and the ages of the Alpine high-pressure metamorphism. Nature 387 (6633), 586–589.
Fu, H., 2020. Analysis of kimberlite emplacement mechanism in the Wafangdian diamond ore field. Acta Geol. Sin. 94, 2640–2649.
Fu, Y., Sun, X., Li, D., Lin, H., 2018. U-Pb geochronology and geochemistry of U-rich garnet from the giant Beiya gold-polymetallic deposit in SW China: constraints on skarn mineralization process. Minerals 8, 128.
Gao, S., Rudnick, R.L., Carlson, R.W., McDonough, W.F., Liu, Y.-S., 2002. Re-Os evidence for replacement of ancient mantle lithosphere beneath the North China Craton. Earth Planet. Sci. Lett. 198 (3-4), 307–322.
Gaspar, M., Knaack, C., Meinert, L.D., Moretti, R., 2008. REE in skarn systems: a LA-ICP-MS study of garnets from the Crown Jewel gold deposit. Geochim. Cosmochim. Acta 72 (1), 185–205.
Gevedon, M., Seman, S., Barnes, J.D., Lackey, J.S., Stockli, D.F., 2018. Unraveling histories of hydrothermal systems via U-Pb laser ablation dating of skarn garnet. Earth Planet. Sci. Lett. 498, 237–246.
Giuliani, A., Phillips, D., Kamenetsky, V.S., Fiorentini, M.L., Farquhar, J., Kendrick, M. A., 2014. Stable isotope (C, O, S) compositions of volatile-rich minerals in kimberlites: a review. Chem. Geol. 374–375, 61–83.
Giuliani, A., Soltys, A., Phillips, D., Kamenetsky, V.S., Maas, R., Goemann, K., Woodhead, J.D., Drysdale, R.N., Griffin, W.L., 2017. The final stages of kimberlite petrogenesis: petrography, mineral chemistry, melt inclusions and Sr-C-O isotope geochemistry of the Bultfontein kimberlite (Kimberley, South Africa). Chem. Geol. 455, 342–356.
Giuliani, A., Pearson, D.G., 2019. Kimberlites: from deep Earth to diamond mines. Elements 15, 377–380.
Ghosh, B., Morishita, T., Ray, J., Tamura, A., Mizukami, T., Soda, Y., Ovung, T.N., 2017. A new occurrence of titanian (hydro)andradite from the Nagaland ophiolite, India: implications for element mobility in hydrothermal environments. Chem. Geol. 457, 47–60.
Grégoire, M., Bell, D.R., Le Roex, A.P., 2003. Garnet lherzolites from the Kaapvaal Craton (South Africa): Trace element evidence for a metasomatic history. J. Petrol. 44, 629–657.
Grew, E.S., Locock, A.J., Mills, S.J., Galuskina, I.O., Galuskin, E.V., Halenius, U., 2013. Nomenclature of the garnet supergroup. Am. Mineral. 98 (4), 785–811.
Griffin, W.L., Batumike, J.M., Greau, Y., Pearson, N.J., Shee, S.R., O'Reilly, S.Y., 2014. Emplacement ages and sources of kimberlites and related rocks in southern Africa: U-Pb ages and Sr-Nd isotopes of groundmass perovskite. Contrib. Mineral. Petrol. 168, 1032.
Grütter, H.S., Gurney, J.J., Menzies, A.H., Winter, F., 2004. An updated classification scheme for mantle-derived garnet, for use by diamond explorers. Lithos 77 (1-4), 841–857.
Guo, X., Navrotsky, A., Kukkadapu, R.K., Engelhard, M.H., Lanzirotti, A., Newville, M., Ilton, E.S., Sutton, S.R., Xu, H., 2016. Structure and thermodynamics of uranium-containing iron garnets. Geochim. Cosmochim. Acta 189, 269–281.
Hardman, M.F., Pearson, D.G., Stachel, T., Sweeney, R.J., 2018. Statistical approaches to the discrimination of crust- and mantle-derived low-Cr garnet - Major-element-based methods and their application in diamond exploration. J. Geochem. Explor. 186, 24–35.
Hayman, P.C., Cas, R.A.F., Johnson, M., 2009. Characteristics and alteration origins of matrix minerals in volcanoclastic kimberlite of the Muskox pipe (Nunavut, Canada). Lithos 112, 473–487.
Heaman, L.M., Phillips, D., Pearson, D.G., 2019. Dating kimberlites: methods and emplacement patterns through time. Elements 15, 399–404.
Hong, J., Zhang, H., Zhai, D., Li, D., Zhang, Y., Liu, J., 2021. The geochronology of the Haobugao skarn Zn-Pb deposit (NE China) using garnet LA-ICP-MS U-Pb dating. Ore Geol. Rev. 139, 104437.
Howarth, G.H., Moore, A.E., Harris, C., van der Meer, Q.H.A., Le Roux, P., 2019. Crustal versus mantle origin of carbonate xenoliths from Kimberley region kimberlites using C-O-Sr-Nd-Pb isotopes and trace element abundances. Geochim. Cosmochim. Acta 266, 258–273.
Huang, Y.-S., Zhao, W.-H., Liu, Y.u., Yang, Y.-H., Tang, G.-Q., Li, Y., Li, X.-H., Zhao, H., Li, Q.-L., 2022. U-Pb dating of andradite-rich garnet by SIMS. J. Anal. At. Spectrom. 37 (5), 1109–1118.
Huggins, F.E., Virgo, D., Huckenholz, H.G., 1977. Titanium-containing silicate garnets. II. The crystal chemistry of melanites and schorlomites. Am. Mineral. 62, 646–665.
Kargin, A.V., Sazonova, L.V., Nosova, A.A., Tretyachenko, V.V., 2016. Composition of garnet and clinopyroxene in peridotite xenoliths from the Grib kimberlite pipe, Arkhangelsk diamond province, Russia: evidence for mantle metasomatism associated with kimberlite melts. Lithos 262, 442–455.
Kamenetsky, V.S., Kamenetsky, M.B., Sharygin, V.V., Golovin, A., 2007. Carbonate-chloride enrichment in fresh kimberlites of the Udachnaya-East pipe, Siberia: a clue to physical properties of kimberlite magmas? Geophys. Res. Lett. 34, L09316.
Kamenetsky, V.S., Golovin, A.V., Maas, R., Giuliani, A., Kamenetsky, M.B., Weiss, Y., 2014. Towards a new model for kimberlite petrogenesis: evidence from unaltered kimberlites and mantle minerals. Earth-Sci. Rev. 139, 145–167.
Kaur, G., Mitchell, R.H., 2013. Mineralogy of the P2-West 'Kimberlite', Wajrakarur kimberlite field, Andhra Pradesh, India: Kimberlite or lamproite? Mineral. Mag. 77 (8), 3175–3196.
Klein-BenDavid, O., Graham Pearson, D., 2009. Origins of subcalcic garnets and their relation to diamond forming fluids — Case studies from Ekati (NWT-Canada) and Murowa (Zimbabwe). Geochim. Cosmochim. Acta 73 (3), 837–855.
Koornneef, J.M., Gress, M.U., Chinn, I.L., Jelsma, H.A., Harris, J.W., Davies, G.R., 2017. Archaean and Proterozoic diamond growth from contrasting styles of large-scale magmatism. Nat. Commun. 8, 648.
Lazarov, M., Brey, G.P., Weyer, S., 2009. Time steps of depletion and enrichment in the Kaapvaal craton as recorded by subcalcic garnets from Finsch (SA). Earth Planet. Sci. Lett. 279 (1-2), 1–10.
Lehmann, B., Storey, C., Mainkar, D., Jeffries, T., 2007. *In-situ* U-Pb dating of titanite in the Tokapal-Bhejripadar kimberlite system, central India. J. Geol. Soc. India 69, 553–556.
Li, D., Tan, C., Miao, F., Liu, Q., Zhang, Y., Sun, X., 2019. Initiation of Zn-Pb mineralization in the Pingbao Pb-Zn skarn district, South China: constraints from U-Pb dating of grossular-rich garnet. Ore Geol. Rev. 107, 587–599.
Li, Q., Chen, F., Wang, X., Li, X., Li, C., 2005. Ultra-low procedural blank and the single-grain mica Rb-Sr isochron dating. Chinese Sci. Bull. 50, 2861–2865.
Li, Q.-L., Wu, F.-Y., Li, X.-H., Qiu, Z.-L., Liu, Y.u., Yang, Y.-H., Tang, G.-Q., 2011. Precisely dating Paleozoic kimberlites in the North China Craton and Hf isotopic constraints on the evolution of the subcontinental lithospheric mantle. Lithos 126 (1-2), 127–134.
Liu, D.Y., Nutman, A.P., Compston, W., Wu, J.S., Shen, Q.H., 1992. Remnants of ≥ 3800 Ma crust in the Chinese part of the Sino-Korean craton. Geology 20, 339–342.
Liu, L., Wu, D., Han, S., Wan, F., Lin, S., Yang, X., 2020. Study of kimberlite-type diamond deposit and its metallogenic model — An example of the primary diamond deposit in the Wafangdian area of Liaoning Province. Acta Geol. Sin. 94, 2650–2665.
Locock, A.J., 2008. An Excel spreadsheet to recast analyses of garnet into end-member components, and a synopsis of the crystal chemistry of natural silicate garnets. Comput. Geosci. 34 (12), 1769–1780.
Lu, F., Wang, Y., Chen, M., Zheng, J., 1998. Geochemical characteristics and emplacement ages of the Mengyin Kimberlites, Shandong Province. China. Int. Geol. Rev. 40 (11), 998–1006.
Lu, F., Zhao, L., Deng, J., Zheng, J., 1995. The discussion on the ages of kimberlitic magma activity in North China Platform. Acta Petrol. Sin. 11, 365–374.
Lu, F., 2010. Multiple-geological events of ancient lithospheric mantle beneath North China Craton: as inferred from peridotite xenoliths in kimberlite. Acta Petrol. Sin. 26, 3177–3188.
Ludwig, K.R., 2012. Isoplot 4.15: A geochronological tookit for Microsoft Excel. Berkeley Geochronology Center Special. Publication 5.
Malkovets, V.G., Griffin, W.L., O'Reilly, S.Y., Wood, B.J., 2007. Diamond, subcalcic garnet, and mantle metasomatism: kimberlite sampling patterns define the link. Geology 35, 339–342.
Malkovets, V.G., Rezvukhin, D.I., Belousova, E.A., Griffin, W.L., Sharygin, I.S., Tretiakova, I.G., Gibsher, A.A., O'Reilly, S.Y., Kuzmin, D.V., Litasov, K.D., Logvinova, A.M., Pokhilenko, N.P., Sobolev, N.V., 2016. Cr-rich rutile: a powerful tool for diamond exploration. Lithos 265, 304–311.
Marks, M.A.W., Coulson, I.M., Schilling, J., Jacob, D.E., Schmitt, A.K., Markl, G., 2008. The effect of titanite and other HFSE-rich mineral (Ti-bearing andradite, zircon,

eudialyte) fractionation on the geochemical evolution of silicate melts. Chem. Geol. 257 (1-2), 153–172.
Mattey, D., Lowry, D., Macpherson, C., 1994. Oxygen isotope composition of mantle peridotite. Earth Planet. Sci. Lett. 128 (3-4), 231–241.
McDonough, W.F., Sun, S.-s., 1995. The composition of the Earth. Chem. Geol. 120 (3-4), 223–253.
Meffre, S., Large, R.R., Scott, R., Woodhead, J., Chang, Z., Gilbert, S.E., Danyushevsky, L.V., Maslennikov, V., Hergt, J.M., 2008. Age and pyrite Pb-isotopic composition of the giant Sukhoi Log sediment-hosted gold deposit. Russia. Geochim. Cosmochim. Acta 72 (9), 2377–2391.
Mezger, K., Hanson, G.N., Bohlen, S.R., 1989. U-Pb systematics of garnet: dating the growth of garnet in the Late Archean Pikwitonei granulite domain at Cauchon and Natawahunan Lakes, Manitoba. Canada. Contrib. Mineral. Petrol. 101 (2), 136–148.
Mezger, K., Rawnsley, C.M., Bohlen, S.R., Hanson, G.N., 1991. U-Pb garnet, sphene, monazite, and rutile ages: implications for the duration of high-grade metamorphism and cooling histories, Adirondack Mts. New York. J. Geol. 99 (3), 415–428.
Millonig, L.J., Albert, R., Gerdes, A., Avigad, D., Dietsch, C., 2020. Exploring laser ablation U-Pb dating of regional metamorphic garnet - The Straits Schist, Connecticut, USA. Earth Planet. Sci. Lett. 552, 116589.
Mitchell, R.H., 1986. Kimberlites: Mineralogy, Geochemistry. Petrology. Plenum Press, New York, pp. 1–442.
Mitchell, R.H., 1995. Kimberlites, Orangeites, and Related Rocks. Plenum Press, New York, pp. 1–410.
Mitchell, R.H., 2008. Petrology of hypabyssal kimberlites: relevance to primary magma compositions. J. Volcanol. Geoth. Res. 174 (1-3), 1–8.
Mitchell, R.H., Giuliani, A., O'Brien, H., 2019. What is a kimberlite? Petrology and mineralogy of hypabyssal kimberlites. Elements 15, 381–386.
Müntener, O., Hermann, J., 1994. Titanian andradite in a metapyroxenite layer from the Malenco ultramafics (Italy): implications for Ti-mobility and low oxygen fugacity. Contrib. Mineral. Petrol. 116, 156–168.
Ni, P., Zhu, R., 2020. Evaluating the diamond potential of kimberlite-hosted diamond deposits from the North China Craton. Acta Geol. Sin. 94, 2557–2573.
Nowicki, T.E., Moore, R.O., Gurney, J.J., Baumgartner, M.C., 2007. Diamonds and associated heavy minerals in kimberlite: a review of key concepts and applications. Dev. Sedimentol. 58, 1235–1267.
Otamendi, J.E., de la Rosa, J.D., Douce, A.E.P., Castro, A., 2002. Rayleigh fractionation of heavy rare earths and yttrium during metamorphic garnet growth. Geology 30, 159–162.
Paton, C., Hellstrom, J., Paul, B., Woodhead, J., Hergt, J., 2011. Iolite: freeware for the visualisation and processing of mass spectrometric data. J. Anal. At. Spectrom. 26, 2508–2518.
Pearson, D.G., Woodhead, J., Janney, P.E., 2019. Kimberlites as geochemical probes of Earth's mantle. Elements 15, 387–392.
Peretyazhko, I.S., Savina, E.A., 2010. Tetrad effects in the rare earth element patterns of granitoid rocks as an indicator of fluoride-silicate liquid immiscibility in magmatic systems. Petrology 18 (5), 514–543.
Piper, J.D.A., Zhang, Q.R., 1997. Palaeomagnetism of Neoproterozoic glacial rocks of the Huabei Shield: the North China Block in Gondwana. Tectonophysics 283 (1-4), 145–171.
Pivin, M., Féménias, O., Demaiffe, D., 2009. Metasomatic mantle origin for Mbuji-Mayi and Kundelungu garnet and clinopyroxene megacrysts (Democratic Republic of Congo). Lithos 112, 951–960.
Rák, Z., Ewing, R.C., Becker, U., 2011. Role of iron in the incorporation of uranium in ferric garnet matrices. Phys. Rev. B 84, 155128.
Ranger, I.M., Heaman, L.M., Pearson, D.G., Muntener, C., Zhuk, V., 2018. Punctuated, long-lived emplacement history of the Renard 2 kimberlite, Canada, revealed by new high precision U-Pb groundmass perovskite dating. Miner. Petrol. 112 (S2), 639–651.
Reguir, E.P., Salnikova, E.B., Yang, P., Chakhmouradian, A.R., Stifeeva, M.V., Rass, I.T., Kotov, A.B., 2021. U-Pb geochronology of calcite carbonatites and jacupirangite from the Guli alkaline complex, Polar Siberia. Russia. Mineral. Mag. 85 (4), 469–483.
Reinhardt, N., Gerdes, A., Beranoaguirre, A., Frenzel, M., Meinert, L.D., Gutzmer, J., Burisch, M., 2022. Timing of magmatic-hydrothermal activity in the Variscan Orogenic Belt: LA-ICP-MS U-Pb geochronology of skarn-related garnet from the Schwarzenberg District, Erzgebirge. Miner. Depos. https://doi.org/10.1007/s00126-021-01084-x.
Rukhlov, A.S., Bell, K., 2010. Geochronology of carbonatites from the Canadian and Baltic Shields, and the Canadian Cordillera: clues to mantle evolution. Miner. Petrol. 98 (1-4), 11–54.
Salnikova, E.B., Stifeeva, M.V., Chakhmouradian, A.R., Glebovitsky, V.A., Reguir, E.P., 2018a. The U-Pb system in schorlomite from calcite-amphobole-pyroxene pegmatite of the Afrikanda Complex (Kola Peninsula). Dokl. Earth Sci. 478 (2), 148–151.
Salnikova, E.B., Stifeeva, M.V., Nikiforov, A.V., Yarmolyuk, V.V., Kotov, A.B., Anisimova, I.V., Sugorakova, A.M., Vrublevskii, V.V., 2018b. Andradite-morimotoite garnets as promising U-Pb geochronometers for dating ultrabasic alkaline rocks. Dokl. Earth Sci. 480 (2), 778–782.
Salnikova, E.B., Chakhmouradian, A.R., Stifeeva, M.V., Reguir, E.P., Kotov, A.B., Gritsenko, Y.D., Nikiforov, A.V., 2019. Calcic garnets as a geochronological and petrogenetic tool applicable to a wide variety of rocks. Lithos 338–339, 141–154.
Samal, A., Srivastava, R.K., Upadhyay, D., 2021. Major, trace, and rare-earth element geochemistry of Nb-V rich andradite-schorlomite-morimotoite garnet from Ambadungar-Saidivasan alkaline carbonatite complex, India: implication for the role of hydrothermal fluid-induced metasomatism. Minerals 11, 756.
Schannor, M., Lana, C., Nicoli, G., Cutts, K., Buick, I., Gerdes, A., Hecht, L., 2021. Reconstructing the metamorphic evolution of the Araçuaí orogen (SE Brazil) using *in situ* U-Pb garnet dating and P-T modelling. J. Metamorph. Geol. 39 (9), 1145–1171.
Scheibner, B., Wörner, G., Civetta, L., Stosch, H.-G., Simon, K., Kronz, A., 2007. Rare earth element fractionation in magmatic Ca-rich garnets. Contrib. Mineral. Petrol. 154 (1), 55–74.
Schmitt, A.K., Zack, T., Kooijman, E., Logvinova, A.M., Sobolev, N.V., 2019. U-Pb ages of rare rutile inclusions in diamond indicate entrapment synchronous with kimberlite formation. Lithos 350-351, 105251.
Schmitz, M.D., Bowring, S.A., 2003. Constraints on the thermal evolution of continental lithosphere from U-Pb accessory mineral thermochronometry of lower crustal xenoliths, southern Africa. Contrib. Mineral. Petrol. 144 (5), 592–618.
Schulze, D., 2003. A classification scheme for mantle-derived garnets in kimberlite: a tool for investigating the mantle and exploring for diamonds. Lithos 71 (2-4), 195–213.
Seman, S., Stockli, D.F., McLean, N.M., 2017. U-Pb geochronology of grossular-andradite garnet. Chem. Geol. 460, 106–116.
Shaikh, A.M., Patel, S.C., Ravi, S., Behera, D., Pruseth, K.L., 2017. Mineralogy of the TK1 and TK4 'kimberlites' in the Timmasamudram cluster, Wajrakarur Kimberlite Field, India: implications for lamproite magmatism in a field of kimberlites and ultramafic lamprophyres. Chem. Geol. 455, 208–230.
Shaikh, A.M., Tappe, S., Bussweiler, Y., Patel, S.C., Ravi, S., Bolhar, R., Viljoen, F., 2020. Clinopyroxene and garnet mantle cargo in kimberlites as probes of Dharwar Craton architecture and geotherms, with implications for post-1.1 Ga lithosphere thinning events beneath southern India. J. Petrol. 61, egaa087.
Shchukina, E.V., Agashev, A.M., Pokhilenko, N.P., 2017. Metasomatic origin of garnet xenocrysts from the V. Grib kimberlite pipe, Arkhangelsk region. NW Russia. Geosci. Front. 8 (4), 641–651.
Shimizu, N., Richardson, S.H., 1987. Trace element abundance patterns of garnet inclusions in peridotite-suite diamonds. Geochim. Cosmochim. Acta 51 (3), 755–758.
Shu, Q., Brey, G.P., 2015. Ancient mantle metasomatism recorded in subcalcic garnet xenocrysts: temporal links between mantle metasomatism, diamond growth and crustal tectonomagmatism. Earth Planet. Sci. Lett. 418, 27–39.
Smit, M.A., Scherer, E.E., Mezger, K., 2013. Lu-Hf and Sm-Nd garnet geochronology: chronometric closure and implications for dating petrological processes. Earth Planet. Sci. Lett. 381, 222–233.
Song, B., Nutman, A.P., Liu, D., Wu, J., 1996. 3800 to 2500 Ma crustal evolution in the Anshan area of Liaoning Province, northeastern China. Precambrian Res. 78, 79–94.
Sparks, R.S.J., Brooker, R.A., Field, M., Kavanagh, J., Schumacher, J.C., Walter, M.J., White, J., 2009. The nature of erupting kimberlite melts. Lithos 1125, 429–438.
Stachel, T., Harris, J.W., 2008. The origin of cratonic diamonds — Constraints from mineral inclusions. Ore Geol. Rev. 34 (1-2), 5–32.
Stifeeva, M.V., Salnikova, E.B., Arzamastsev, A.A., Kotov, A.B., Grozdev, V.Y., 2020. Calcic garnets as a source of information on the age of ultramafic alkaline intrusions in the Kola magmatic province. Petrology 28 (1), 62–72.
Tang, Y., Gao, J., Lan, T., Cui, K., Han, J., Zhang, X., Chen, Y., Chen, Y., 2021. *In situ* low-U garnet U-Pb dating by LA-SF-ICP-MS and its application in constraining the origin of Anji skarn system combined with Ar-Ar dating and Pb isotopes. Ore Geol. Rev. 130, 103970.
Tappe, S., Jenner, G.A., Foley, S.F., Heaman, L., Besserer, D., Kjarsgaard, B.A., Ryan, B., 2004. Torngat ultramafic lamprophyres and their relation to the North Atlantic Alkaline Province. Lithos 76 (1-4), 491–518.
Tappe, S., Foley, S.F., Jenner, G.A., Kjarsgaard, B.A., 2005. Integrating ultramafic lamprophyres into the IUGS classification of igneous rocks: rationale and implications. J. Petrol. 46, 1893–1900.
Tappe, S., Foley, S.F., Jenner, G.A., Heaman, L.M., Kjarsgaard, B.A., Romer, R.L., Stracke, A., Joyce, N., Hoefs, J., 2006. Genesis of ultramafic lamprophyres and carbonatites at Aillik Bay, Labrador: a consequence of incipient lithospheric thinning beneath the North Atlantic craton. J. Petrol. 47, 1261–1315.
Tappe, S., Foley, S.F., Kjarsgaard, B.A., Romer, R.L., Heaman, L.M., Stracke, A., Jenner, G.A., 2008. Between carbonatite and lamproite — Diamondiferous Torngat ultramafic lamprophyres formed by carbonate-fluxed melting of cratonic MARID-type metasomes. Geochim. Cosmochim. Acta 72 (13), 3258–3286.
Tappe, S., Steenfelt, A., Heaman, L.M., Simonetti, A., 2009. The newly discovered Jurassic Tikiusaaq carbonatite-aillikite occurrence, West Greenland, and some remarks on carbonatite-kimberlite relationships. Lithos 112, 385–399.
Tappe, S., Pearson, D.G., Nowell, G., Nielsen, T., Milstead, P., Muehlenbachs, K., 2011. A fresh isotopic look at Greenland kimberlites: cratonic mantle lithosphere imprint on deep source signal. Earth Planet. Sci. Lett. 305 (1-2), 235–248.
Tappe, S., Kjarsgaard, B.A., Kurszlaukis, S., Nowell, G.M., Phillips, D., 2014. Petrology and Nd-Hf isotope geochemistry of the Neoproterozoic Amon kimberlite sills, Baffin Island (Canada): Evidence for deep mantle magmatic activity linked to supercontinent cycles. J. Petrol. 55, 2003–2042.
Tappe, S., Romer, R.L., Stracke, A., Steenfelt, A., Smart, K.A., Muehlenbachs, K., Torsvik, T.H., 2017. Sources and mobility of carbonate melts beneath cratons, with implications for deep carbon cycling, metasomatism and rift initiation. Earth Planet. Sci. Lett. 466, 152–167.

Tappe, S., Smart, K., Torsvik, T., Massuyeau, M., de Wit, M., 2018a. Geodynamics of kimberlites on a cooling Earth: clues to plate tectonic evolution and deep volatile cycles. Earth Planet. Sci. Lett. 484, 1–14.
Tappe, S., Dongre, A., Liu, C.Z., Wu, F.Y., 2018b. 'Premier' evidence for prolonged kimberlite pipe formation and its influence on diamond transport from deep Earth. Geology 46, 843–846.
Tappe, S., Shaikh, A.M., Wilson, A.H., Stracke, A., 2022. Evolution of ultrapotassic volcanism on the Kaapvaal craton: deepening the orangeite versus lamproite debate. Geol. Soc. London. Spec. Pub. 513 (1), 17–44.
Tompkins, L.A., Meyer, S.P., Han, Z., Hu, S., 1998. Petrology and geochemistry of kimberlites from Liaoning and Shandong Provinces, China. International Kimberlite Conference: Extended Abstracts 7, 917–919.
Vermeesch, P., 2018. IsoplotR: a free and open toolbox for geochronology. Geosci. Front. 9 (5), 1479–1493.
Hode Vuorinen, J., Hålenius, U., Whitehouse, M.J., Mansfeld, J., Skelton, A.D.L., 2005. Compositional variations (major and trace elements) of clinopyroxene and Ti-andradite from pyroxenite, ijolite and nepheline syenite, Alnö Island, Sweden. Lithos 81 (1-4), 55–77.
Wafforn, S., Seman, S., Kyle, J.R., Stockli, D., Leys, C., Sonbait, D., Cloos, M., 2018. Andradite garnet U-Pb geochronology of the big Gossan skarn, Ertsberg-Grasberg mining district. Indonesia. Econ. Geol. 113, 769–778.
Wang, S., Zheng, J., Han, S., Wang, J., 2020. Petrography and petrogenesis of porphyritic kimberlite from South Liaoning. Acta Geol. Sin. 94, 2676–2686.
Wang, W., Sueno, S., Takahashi, E., Yurimoto, H., Gasparik, T., 2000. Enrichment processes at the base of the Archean lithospheric mantle: observations from trace element characteristics of pyropic garnet inclusions in diamonds. Contrib. Mineral. Petrol. 139 (6), 720–733.
Willigers, B.J.A., Mezger, K., Baker, J.A., 2004. Development of high precision Rb-Sr phlogopite and biotite geochronology; an alternative to $^{40}Ar/^{39}Ar$ tri-octahedral mica dating. Chem. Geol. 213 (4), 339–358.
Wilson, M.R., Kjarsgaard, B.A., Taylor, B., 2007. Stable isotope composition of magmatic and deuteric carbonate phases in hypabyssal kimberlite, Lac de Gras field, Northwest Territories. Canada. Chem. Geol. 242 (3-4), 435–454.
Woolley, A.R., Bergman, S.C., Edgar, A.D., Le Bas, M.J., Mitchell, R.H., Rock, N.M.S., Smith, B.H.S., 1996. Classification of lamprophyres, lamproites, kimberlites, and the kalsilitic, melilitic, and leucitic rocks. Can. Mineral. 34, 175–186.
Wu, F.-Y., Walker, R.J., Ren, X.-W., Sun, D.-Y., Zhou, X.-H., 2003. Osmium isotopic constraints on the age of lithospheric mantle beneath northeastern China. Chem. Geol. 196 (1-4), 107–129.
Xiao, X., Zhou, T.F., White, N.C., Zhang, L.J., Fan, Y., Wang, F.Y., Chen, X.F., 2018. The formation and trace elements of garnet in the skarn zone from the Xinqiao Cu-S-Fe-Au deposit, Tongling ore district, Anhui Province, Eastern China. Lithos 302–303, 467–479.
Yan, S., Zhou, R., Niu, H., Feng, Y., Nguyen, A.D., Zhao, Z., Yang, W., Dong, Q., Zhao, J., 2020. LA-MC-ICP-MS U-Pb dating of low-U garnets reveals multiple episodes of skarn formation in the volcanic-hosted iron mineralization system, Awulale belt, Central Asia. Geol. Soc. Am. Bull. 132, 1031–1045.
Yang, Y.-H., Wu, F.-Y., Wilde, S.A., Liu, X.-M., Zhang, Y.-B., Xie, L.-W., Yang, J.-H., 2009. *In situ* perovskite Sr-Nd isotopic constraints on the petrogenesis of the Ordovician Mengyin kimberlites in the North China Craton. Chem. Geol. 264 (1-4), 24–42.
Yang, Y.-H., Wu, F.-Y., Yang, J.-H., Mitchell, R.H., Zhao, Z.-F., Xie, L.-W., Huang, C., Ma, Q., Yang, M., Zhao, H., 2018. U-Pb age determination of schorlomite garnet by laser ablation inductively coupled plasma mass spectrometry. J. Anal. At. Spectrom. 33 (2), 231–239.
Zhang, H., Menzies, M.A., Lu, F., Zhou, X., 2000. Major and trace element studies on garnets from Palaeozoic kimberlite-borne mantle xenoliths and megacrysts from the North China craton. Sci. China Ser. D 43 (4), 423–430.
Zhang, H., Yang, Y., 2007. Emplacement age and Sr-Nd-Hf isotopic characteristics of the diamondiferous kimberlites from the eastern North China Craton. Acta Petrol. Sin. 23, 285–294.
Zhang, H.-F., Zhou, M.-F., Sun, M., Zhou, X.-H., 2010. The origin of Mengyin and Fuxian diamondiferous kimberlites from the North China Craton: implication for Palaeozoic subducted oceanic slab-mantle interaction. J. Asian Earth Sci. 37 (5-6), 425–437.
Zhang, S., Chen, H., Shu, Q., Zhang, Y., Chu, G., Cheng, J., Tian, J., 2019. Unveiling growth histories of multi-generational garnet in a single skarn deposit via newly-developed LA-ICP-MS U-Pb dating of grandite. Gondwana Res. 73, 65–76.
Zhao, D., Zhang, Y., Essene, E.J., 2015. Electron probe microanalysis and microscopy: principles and applications in characterization of mineral inclusions in chromite from diamond deposit. Ore Geol. Rev. 65, 733–748.
Zhao, G., Sun, M., Wilde, S.A., Li, S., 2005. Late Archean to Paleoproterozoic evolution of the North China Craton: key issues revisited. Precambrian Res. 136 (2), 177–202.
Zhao, G., Wilde, S.A., Cawood, P.A., Sun, M., 2002. SHRIMP U-Pb zircon ages of the Fuping Complex: implications for Late Archean to Paleoproterozoic accretion and assembly of the North China Craton. Am. J. Sci. 302, 191–226.
Zhao, G., Zhai, M., 2013. Lithotectonic elements of Precambrian basement in the North China Craton: review and tectonic implications. Gondwana Res. 23 (4), 1207–1240.
Zheng, J., Griffin, W.L., O'Reilly, S.Y., Lu, F., Yu, C., Zhang, M., Li, H., 2004. U-Pb and Hf-isotope analysis of zircons in mafic xenoliths from Fuxian kimberlites: evolution of the lower crust beneath the North China Craton. Contrib. Mineral. Petrol. 148 (1), 79–103.
Zhu, R.Z., Ni, P., Ding, J.Y., Wang, D.Z., Ju, Y., Kang, N., Wang, G.G., 2017. Petrography, chemical composition, and Raman spectra of chrome spinel: constraints on the diamond potential of the No. 30 pipe kimberlite in Wafangdian. North China Craton. Ore Geol. Rev. 91, 896–905.
Zhu, R.Z., Ni, P., Ding, J.Y., Wang, G.G., 2019a. Geochemistry of magmatic and xenocrystic spinel in the No. 30 kimberlite pipe (Liaoning Province North China Craton): constraints on diamond potential. Minerals 9, 382.
Zhu, R.Z., Ni, P., Ding, J.Y., Wang, G.G., Fan, M.S., Li, S.N., 2019b. Metasomatic processes in the lithospheric mantle beneath the No. 30 kimberlite (Wafangdian region, North China Craton). Can. Mineral. 57, 499–517.
Zhu, R.-Z., Ni, P., Wang, G.-G., Ding, J.-Y., Kang, N., 2022. Temperature and oxygen state of kimberlite magma from the North China Craton and their implication for diamond survival. Miner. Depos. 57 (2), 301–318.